

# Symmetry breaking and spectral structure of the interacting Hatano-Nelson model

Song-Bo Zhang,<sup>1</sup> M. Michael Denner,<sup>1</sup> Tomáš Bzdušek,<sup>2,1</sup> Michael A. Sentef,<sup>3</sup> and Titus Neupert<sup>1</sup>

<sup>1</sup>*Department of Physics, University of Zürich, Winterthurerstrasse 190, 8057, Zürich, Switzerland*

<sup>2</sup>*Condensed Matter Theory Group, Paul Scherrer Institute, 5232 Villigen PSI, Switzerland*

<sup>3</sup>*Max Planck Institute for the Structure and Dynamics of Matter,  
Luruper Chaussee 149, 22761 Hamburg, Germany*

(Dated: September 7, 2022)

We study the Hatano-Nelson model, i.e., a one-dimensional non-Hermitian chain of spinless fermions with nearest-neighbor nonreciprocal hopping, in the presence of repulsive nearest-neighbor interactions. At half-filling, we find two  $\mathcal{PT}$  transitions, as the interaction strength increases. The first transition is marked by an exceptional point between the first and the second excited state in a finite-size system and is a first-order symmetry-breaking transition into a charge-density wave regime. Persistent currents characteristic of the Hatano-Nelson model abruptly vanish at the transition. The second transition happens at a critical interaction strength that scales with the system size and can thus only be observed in finite-size systems. It is characterized by a collapse of all energy eigenvalues onto the real axis. We further show that in a strong interaction regime, but away from half-filling, the many-body spectrum shows point gaps with nontrivial winding numbers, akin to the topological properties of the single-particle spectrum of the Hatano-Nelson chain, which indicates the skin effect of extensive many-body eigenstates under open boundary conditions. Our results can be applied to other models such as the non-Hermitian Su-Schrieffer-Heeger-type model, and contribute to an understanding of fermionic many-body systems with non-Hermitian Hamiltonians.

*Introduction*—Non-Hermitian topological phases constitute one of the most recent active research fields in condensed matter, cold atom, and photonic physics [1–33]. They have been experimentally realized in different platforms of high controllability [34–50]. So far, most previous efforts have been devoted to single-particle physics, with no or only perturbative many-body interactions. It is well known that in Hermitian systems strong interactions among particles give rise to many exotic phenomena, such as unconventional superconductivity, Mott insulators, and density-wave ordering [51–53]. Thus, it is of fundamental interest to explore non-Hermitian phenomena in many-body systems with strong interactions [54–79]. Most of the existing studies on this subject are focused on the issues of non-Hermitian many-body localization [56–59] and the non-Hermitian skin effect [61–69]. However, many-body interaction effects, especially on bulk fermionic properties, remain largely unexplored even in simple models.

In this Letter, we study the Hatano-Nelson model of spinless fermions, a prototypical one-dimensional non-Hermitian system with nearest-neighbor nonreciprocal hopping [80], in a ring geometry and under the presence of the Pauli principle and strong Coulomb interactions. At half-filling [Fig. 1(a)], we find that as the interaction strength increases, the imaginary energies of the many-body spectrum are substantially suppressed, giving rise to two  $\mathcal{PT}$  transitions. The first transition is marked by an exceptional point between two lowest excited states (LES) [81] of a finite-size system [see a sketch in Fig. 1(b)]. By employing exact diagonalization, we show that this transition corresponds to a first-order quantum phase transition of the ground state from a gapless phase to a gapped charge-density wave (CDW) that

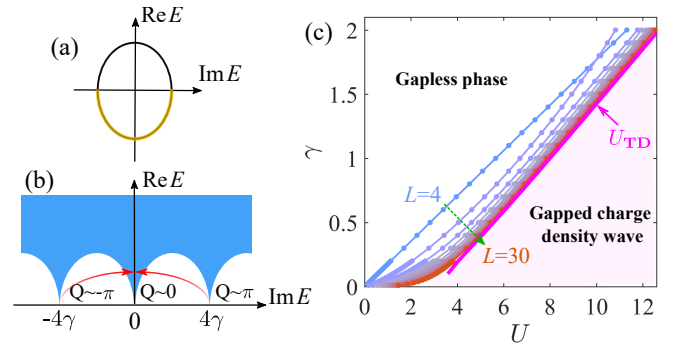


Fig. 1. (a) Single-particle spectrum and (b) low-excitation-energy many-body spectrum at half-filling in the absence of interactions. The yellow arc denotes the filled states. Two LES have momenta  $Q = \pm\pi$  and identical  $\text{Re}(E)$  but opposite  $\text{Im}(E) \approx \pm 4i\gamma$ . By increasing the interaction strength  $U$  to a critical value  $U_c$ , the two LES collapse onto the real axis, as sketched by the arrows. (c) Phase diagram against  $\gamma$  and  $U$ . The gapless phase is adiabatically connected to the Hatano-Nelson model at  $U = 0$ , while the CDW phase is smoothly connected to the CDW phase with  $\gamma = 0$  and finite  $U$ . The magenta line is the extrapolated  $U_{\text{TD}}$  in the TDL. It demarcates the gapless regime and the gapped CDW regime.

breaks translation symmetry spontaneously [Fig. 1(c)]. Moreover, it features a sudden disappearance of the characteristic persistent current of the Hatano-Nelson model in a low-temperature regime. The second transition corresponds to a full collapse of the many-body spectrum onto the real axis. Its critical interaction strength, however, increases as the system size grows. Thus, it can only be observed in finite-size systems.

For finite doping away from half-filling, the spectrum stratifies into clusters with states of a different number of

simultaneously occupied nearest-neighbor sites. The energy clusters have nonzero extents along imaginary axis being largely unaffected by interactions. Furthermore, they exhibit point gaps with nontrivial winding numbers, thus indicating the skin effect of many-body states in the presence of open boundaries [13–15, 82], also for strong interactions. At half-filling, in contrast, the spectrum shrinks to open lines under strong interactions. Accordingly, the many-body states extend over the whole lattice chain with open boundaries.

*Interacting Hatano-Nelson model.*—We consider the interacting Hatano-Nelson model of spinless fermions described by

$$\hat{H} = \sum_{\ell} [(t + \gamma)\hat{c}_{\ell}^{\dagger}\hat{c}_{\ell+1} + (t - \gamma)\hat{c}_{\ell+1}^{\dagger}\hat{c}_{\ell} + U\hat{n}_{\ell}\hat{n}_{\ell+1}], \quad (1)$$

where  $\hat{c}_{\ell}^{\dagger}$  ( $\hat{c}_{\ell}$ ) is the creation (annihilation) operator of a fermion at lattice site  $\ell$ , and  $\hat{n}_{\ell} = \hat{c}_{\ell}^{\dagger}\hat{c}_{\ell}$  is the fermion number operator with eigenvalues  $\{0, 1\}$ . The fermionic operators  $\hat{c}_{\ell}^{\dagger}$  and  $\hat{c}_{\ell}$  obey the anticommutation relations, thus imposing the Pauli principle to the system [84]. The real parameters  $t$  and  $\gamma$  denote the reciprocal and non-reciprocal components of the hopping between neighboring sites, respectively [85]. The last term describes the Coulomb interaction with strength  $U \geq 0$  between two fermions at adjacent sites. Without loss of generality, we set  $t > 0$  to be our unit of energy.

To investigate bulk many-body properties, we consider the system in a ring geometry with  $L$  sites and  $N$  particles. For periodic boundary conditions (PBC) or anti-PBC, the system respects a combined space-time-reversal ( $\mathcal{PT}$ ) symmetry [84]; thus, the eigenenergies of the system are either real or come in complex-conjugate pairs. For single particles without interactions, the spectrum reduces to a closed orbit with a point gap [Fig 1(a)], resulting in the non-Hermitian skin effect of single-particle states at open boundaries [4–6]. Moreover, the system has a particle-hole symmetry [84]. Thus, the spectrum for  $N$  particles is essentially the same (up to an overall shift in energy) as that for  $L - N$  particles. Both of these spectral relations are reproduced by our exact-diagonalization calculations presented below.

*Low-energy  $\mathcal{PT}$  transition and phase diagram.*—It is instructive to first analyze the case without interactions ( $U = 0$ ). In this case, the many-body spectrum displays a scatter distribution pattern centered at the origin of the complex-energy plane. When  $n_{\text{cl}} = \min(N, L - N) \gg 1$ , its extent along real and imaginary axes can be estimated as  $\Xi_{\text{R}} \approx t\alpha_{\{N, L\}}$  and  $\Xi_{\text{I}} \approx \gamma\alpha_{\{N, L\}}$ , respectively, where  $\alpha_{\{N, L\}} = 2L \sin(\pi n_{\text{cl}}/L)/\pi$  [84]. Clearly, the spectrum is larger when the system is larger and filled closer to half-filling. For fixed finite  $n_{\text{cl}} (\ll L)$ , however, its extent is approximately independent of  $L$  and determined by  $\alpha_{\{N, L\}} \approx 2n_{\text{cl}}$ .

More intriguing features arise when the interaction is present. We first consider the half-filled ( $N = L/2$ )

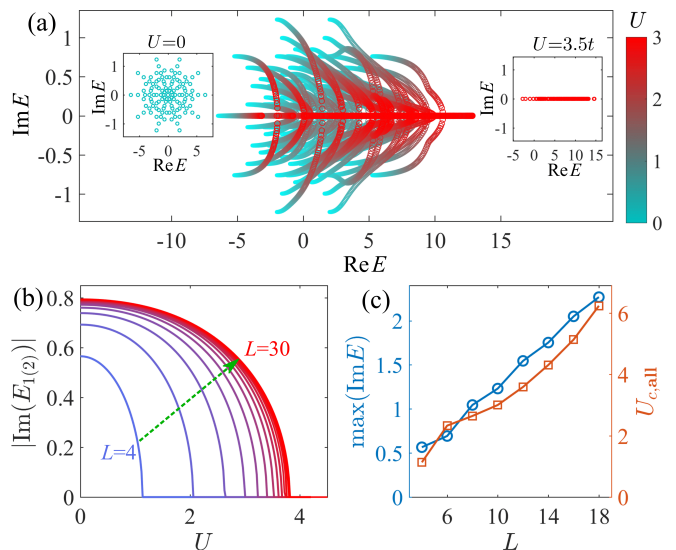


Fig. 2. (a) Flow of the spectrum at half-filling as  $U$  increases from 0 (cyan) to  $3.5t$  (red). Insets: spectra at  $U = 0$  and  $U = 3t$ , respectively. All eigenenergies become real when  $U \geq U_{c,\text{all}}$ . (b)  $|\text{Im}(E_{1(2)})|$  as a function of  $U$  for increasing  $L$ . The dependence of  $|\text{Im}(E_{1(2)})|$  on  $U$  converges to the red curve as  $L$  grows. (c) Maximum imaginary energy  $\max(\text{Im} E)$  (blue) and  $U_{c,\text{all}}$  (orange) as functions of  $L$ . Both quantities diverge as  $L \rightarrow \infty$ . We consider  $L = 10$  in (a),  $\gamma = 0.2t$  in all panels, adopt (anti-)PBC for odd (even)  $N$ .

scenario and show that a  $\mathcal{PT}$  transition between  $\mathcal{PT}$ -symmetry-broken and -unbroken phases occurs at low excitation energies, as  $U$  increases. As illustrated in Fig. 1(b) and the inset of Fig. 2(a), at  $U = 0$ , there is one ground state with real energy  $E_0$  and two LES with complex-conjugate energies  $E_2 = E_1^*$  in systems with odd (even)  $N$  and (anti-)PBC. When  $L \gg 1$ , we have  $E_0 \approx 2tL/\pi$  and  $E_1 = E_2^* \approx E_0 + 4t \sin(\pi/L) + 4i\gamma \cos(\pi/L)$ . As  $U$  increases, we find that the energies of the LES approach each other and merge at an exceptional point on the real axis at a critical strength  $U = U_c$ , and split along the real axis for  $U > U_c$ .

To better understand the *low-energy  $\mathcal{PT}$  transition*, we determine  $U_c$  for varying  $\gamma$  and increasing  $L$  [Figs. 1(c) and 2(b)]. Evidently,  $|\text{Im}(E_{1(2)})|$  decays monotonically with increasing  $U (< U_c)$  and completely vanishes when  $U > U_c$ . As  $L$  grows, the dependence of  $|\text{Im}(E_{1(2)})|$  on  $U$  converges to a curve [red line in Fig. 2(b)]. In the thermodynamic limit (TDL)  $L \rightarrow \infty$ ,  $U_c$  converges to a finite value  $U_{\text{TD}}$ . Specifically, for fixed  $\gamma$ ,  $U_c$  shows a power-law scaling as  $L$  grows, i.e.,

$$U_c = U_{\text{TD}} - \beta L^{-\alpha}, \quad (2)$$

where  $\alpha$  and  $\beta$  are positive numbers depending on  $\gamma$ . This feature enables us to extrapolate  $U_{\text{TD}}$ . The phase diagram parametrized by  $U$  and  $\gamma$  is given in Fig. 1(c), where the red line is  $U_{\text{TD}}$  which marks the phase boundary in the TDL [86]. We observe that  $U_{\text{TD}}$  grows monotonically

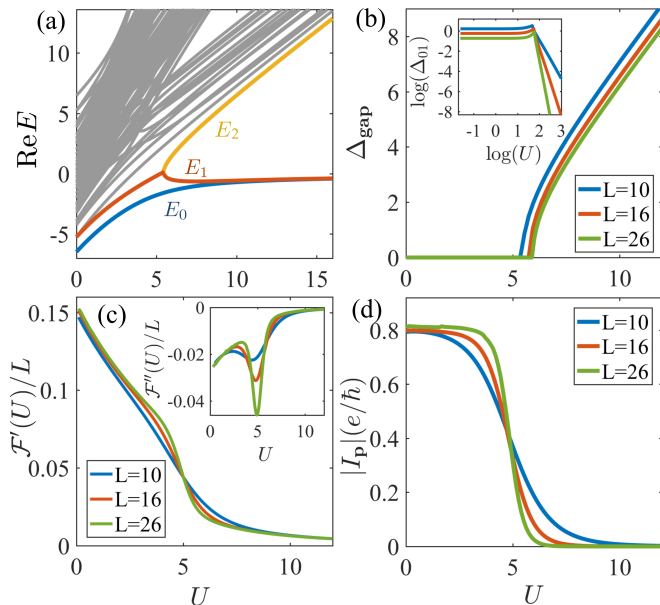


Fig. 3. (a) Real part of the spectrum at half-filling as a function of  $U$ . Three lowest energy levels are respectively denoted as  $E_0$ ,  $E_1$  and  $E_2$ . (b)  $\Delta_{\text{gap}}$  as a function of  $U$ . Inset:  $\log(\Delta_{01})$  as a function of  $\log(U)$ . (c) The first and second derivatives of the free energy as functions of  $U$ . (d)  $|I_p|$  (in units of  $e/h$ ) as a function of  $U$ . We consider  $\gamma = 0.6t$  in all panels,  $L = 10$  in (a),  $k_B T = 0.4t$  and 50 lowest- $\text{Re}(E)$  eigenstates in (c) and (d).

with  $\gamma$ , indicating that the  $\mathcal{PT}$  transition occurs even in the TDL and for ultrastrong nonreciprocity ( $|\gamma| \geq t$ ). More details of the calculation are given in the Supplemental Material [84].

To further understand the physics behind the phase diagram, we analyze the real part of the low-excitation-energy spectrum [Fig. 3(a)]. For  $U < U_c$ , the two LES are degenerate in real energy. The finite-size level spacing  $\Delta_{01} \equiv \text{Re}(E_1 - E_0)$  is approximately constant [ $\approx 4t \sin(2\pi/L)$ ] for a wide range of  $U$  and increases subtly when approaching  $U_c$  [inset of Fig. 3(b)]. However,  $\Delta_{01}$  decreases as  $L$  grows and it vanishes in the TDL, indicating a gapless phase when  $U < U_c$ . For  $U > U_c$ , the LES have vanishing imaginary energy while being split in real energy. Upon further increasing  $U$ , the energy splitting  $\Delta_{\text{gap}} \equiv \text{Re}(E_2 - E_1)$  increases whereas  $\Delta_{01}$  decreases sharply [Fig. 3(b)]. More explicitly,  $\Delta_{01}$  follows a power-law dependence  $\Delta_{01} \propto U^{1-L/2}$  on  $L$ . Thus, in large systems, one of the LES rapidly becomes degenerate with the ground state and separated from the excited states by a large gap  $\Delta_{\text{gap}}$ , implying a transition of the system into a gapped regime. The degenerate ground states break translation symmetry spontaneously, forming a CDW with long-range density-density correlation [84]. The  $\mathcal{PT}$  transition may also be related to the breakdown of the Mott insulator which instead considers two spin species and on-site interactions [83].

*Free energy and persistent current.*—Next, we consider the free energy of the system, which reads  $\mathcal{F} = -k_B T \log(\sum_j e^{-E_j/k_B T})$ , where  $T$  is the temperature,  $k_B$  is the Boltzmann constant and  $\sum_j$  sums over all eigenenergies. Since the eigenenergies are real or come in complex-conjugate pairs due to the  $\mathcal{PT}$  symmetry,  $\mathcal{F}$  is always purely real. At low temperatures,  $\mathcal{F}$  is determined mainly by the low- $\text{Re}(E)$  eigenstates in an energy window of magnitude  $k_B T$ . As discussed above, in the TDL, the system is gapless for  $U < U_c$ , whereas it quickly develops a large energy gap after  $U > U_c$ . As a result,  $\mathcal{F}$  and its derivatives (with respect to  $U$ ) change significantly at  $U_c$ , provided that  $\Delta_{01} < k_B T \ll U_c$ . In Fig. 3(c), we calculate the first and second derivatives of  $\mathcal{F}$  at low temperatures as functions of  $U$ . We observe that for  $L/2 \gg 1$ , the first derivative  $\mathcal{F}' \equiv d\mathcal{F}/dU$  shows a sudden drop while the second derivative  $\mathcal{F}'' \equiv d^2\mathcal{F}/dU^2$  diverges at  $U_c$ . These features are more pronounced in larger systems, suggesting that the low-energy  $\mathcal{PT}$  transition is of first order. This is in sharp contrast to the Hermitian limit ( $\gamma = 0$ ), where the transition is of Berezinskii-Kosterlitz-Thouless type [87–89] (see also [84]).

In a metallic ring, a persistent current  $I_p$  can be induced as the response of  $\mathcal{F}$  to a small change of magnetic flux  $\phi$  through the ring, i.e.,  $I_p = -(e/h)\partial\mathcal{F}/\partial\phi$  [90]. Notably, by virtue of its non-Hermitian hopping, the Hatano-Nelson model supports an imaginary current  $I_p$  at zero flux for  $U < U_c$  [91]. In the TDL and for  $U = 0$  and  $T = 0$ ,  $I_p$  can be derived as  $I_p = 4ie\gamma/h$  [84]. Moreover, when  $\Delta_{01} < k_B T \ll U_c$ ,  $I_p$  is approximately constant for  $U < U_c$ , whereas it suddenly drops to zero for  $U > U_c$ , as shown numerically in Fig. 3(d). For small  $U$ ,  $I_p$  saturates for large  $L$ , and it exhibits a sudden drop at the transition that sharpens with increasing  $L$ . This is in contrast to the persistent current in Hermitian systems that requires a finite flux and vanishes in the TDL [92]. Note that the imaginary current characterizes the delocalization of eigenstates [80]. The sudden disappearance of  $I_p$  thus constitutes another indicator of the metal-insulator transition in the low- $\text{Re}(E)$  regime.

*$\mathcal{PT}$  transition in the full spectrum.*—The full many-body spectrum can also exhibit a  $\mathcal{PT}$  transition at half-filling. As shown in Fig. 2(a) for  $|\gamma| < t$ , the imaginary part of the spectrum is dramatically suppressed by increasing  $U$  and, more remarkably, all eigenenergies collapse onto the real axis after a critical strength  $U_{c,\text{all}}$  in a system with odd (even)  $N$  and (anti-)PBC. This *full*  $\mathcal{PT}$  transition can be understood as follows. In the presence of Coulomb interactions, the many-body Fock states of the system acquire different Coulomb potentials determined by their occupation configurations [93], forming different groups with different Coulomb potentials (we term them Fock components for convenience). At half-filling, we find that the imaginary energies of the spectrum mainly stem from the nonreciprocal hopping between different Fock components. By increasing  $U$ , the

energy separation between the Fock components grows and the coupling between them becomes weaker. Thus, the imaginary energies are suppressed. We stress that the complex-real transition discovered here emerges in the many-body spectrum and is driven by two-particle interactions, distinctively different from the complex-real transition in the single-particle spectrum driven by disorders [80].

The value of  $U_{c,\text{all}}$  depends on the system size  $L$  and nonreciprocity  $\gamma$ . In larger systems, there are more excited states with larger imaginary energies at  $U = 0$ . When  $L \gg 1$ , the maximum imaginary energy  $\max[\text{Im}(E)]$  is approximately  $2\gamma L/\pi$ , which grows linearly with  $L$  [in contrast to the imaginary energies of LES, which is bounded by  $\text{Im}(E_1) < 4\gamma$ ]. Thus, in order to completely suppress the imaginary energies, a stronger  $U_{c,\text{all}}$  is required. Explicitly,  $U_{c,\text{all}}$  scales with the system size and can thus only be observed in finite-size systems [Fig. 2(c)]. Similarly, for larger  $\gamma$ , we have larger imaginary energies at  $U = 0$  and thus larger  $U_{c,\text{all}}$ .

For  $|\gamma| \geq t$ , the imaginary energies stem not only from the nonreciprocal hopping between different Fock components but also from those between the states within the same component. Since these hoppings are not suppressed by the  $U$ -driven separation of the Fock components, the imaginary energies are a robust property, and the full  $\mathcal{PT}$  transition is not realized at any finite  $U$ .

We also note that the above-discussed  $\mathcal{PT}$  transitions occur only in the case with odd (even)  $N$  and (anti-)PBC while they are absent in the case with even (odd)  $N$  and (anti-)PBC. However, we expect the phase diagram in the TDL to be identical for all the cases [84].

*Spectral clusters with nontrivial windings away from half-filling.*—Finally, we turn to the non-half-filled case where additional interesting properties emerge in the presence of strong interactions. First, the many-body spectrum is substantially redistributed and dispersed from a connected area in the complex-energy plane into  $n_{\text{cl}}$  clusters when  $U > \Xi_{\text{R}}$  [Figs. 4(a-b)]. Each cluster corresponds to a Fock component with a given Coulomb potential. Accordingly, the clusters are centered respectively around the energies  $\varepsilon_s = (N-s)U$  with  $1 \leq s \leq n_{\text{cl}}$  labeling the clusters. Second, each cluster by itself also exhibits a symmetric pattern in the complex-energy plane. Due to particle-hole symmetry, the clusters for  $L-N$  particles are the same as those for  $N$  particles up to an overall energy shift  $|2N-L|U$ . Finally, in the non-half-filled case, the imaginary energies always comprise nonreciprocal hopping between states within the same Fock component. Thus, the clusters are insensitive to  $U$  in the strong  $U$  regime, except for the cluster centered at  $\varepsilon_1$ , whose extent shrinks with increasing  $U$ .

The spectral clusters can be characterized by nontrivial topological invariants. To see this, for finite-size systems, we introduce a twist angle  $\phi$  to the PBC [8]. When  $\phi$  increases from 0 to  $2\pi$ , all the eigenenergies belonging

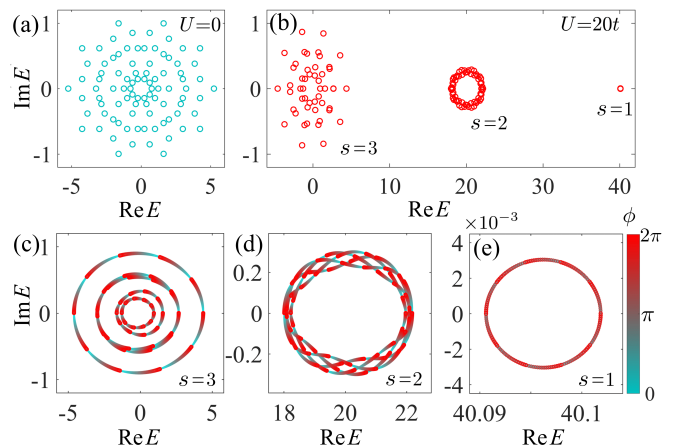


Fig. 4. Many-body spectrum at (a)  $U = 0$  and (b)  $20t$ , respectively. (c–e) Movement of the spectral clusters as  $\phi$  varies from 0 (cyan) to  $2\pi$  (red). Parameters:  $L = 10$ ,  $N = 3$  and  $\gamma = 0.2t$ .

to cluster  $s$  wind around the center  $\varepsilon_s$  in one direction determined by  $\text{sgn}(\gamma)$  [Figs. 4(c–e)]. Thus, a nontrivial winding number can be found as

$$\nu_s = \int_0^{2\pi} \frac{d\phi}{2\pi i} \sum_j \partial_\phi \log\{E_j(\phi) - \varepsilon_s\}, \quad (3)$$

where  $\sum_j$  sums over all eigenenergies. Specifically, we find  $\nu_1 = \text{sgn}(\gamma)N$  for  $s = 1$ . For other clusters  $s \geq 2$ ,  $\nu_s$  depend also on  $L$  and diverge as  $L \rightarrow \infty$ . Furthermore, for fixed  $N$  in the TDL, the clusters form at least one continuous orbit of eigenenergies surrounding each energy center [84]. Hence, the winding numbers of these orbits can also define nontrivial topological invariants. Note that the winding numbers defined for the spectral clusters are general for strong interactions  $U > \Xi_{\text{R}}$  [94]. The spectrum under open boundary conditions collapses to open lines without windings. The nonzero winding numbers under PBC indicate the localization of the many-body eigenstates at the Fock basis states with particles accumulated at an open boundary (if present) and hence the localization of the many-body eigen wavefunctions towards the boundary [62, 69, 95], regardless of the Pauli principle and strong interactions in the system. We show this explicitly in the supplemental materials [84]. Our work thus constitutes a many-body interacting generalization of the spectral winding number [13–15, 82] used to characterize the non-Hermitian skin effect.

By contrast, at half-filling, the spectrum of a finite-size system under PBC shrinks to open lines in the strong interaction regime, as discussed before. In this case, the spectral winding numbers become ill-defined. The many-body wavefunctions extend over the whole lattice even with boundaries [84].

*Summary and discussion.*—We have revealed two  $\mathcal{PT}$  transitions in the interacting Hatano-Nelson model at

half-filling upon increasing interaction strength: one is marked by an exceptional point between two LES, and the other one is characterized by a full collapse of the many-body spectrum onto the real axis. The former transition corresponds to a symmetry-breaking transition into a gapped CDW regime and features a sudden disappearance of the persistent current at low temperatures. We have further shown that with strong interactions but away from half-filling, the many-body spectrum stratifies into multiple clusters characterized by nontrivial winding numbers.

It is important to note that our main results from the Hatano-Nelson model are general. They can also be applied to other models, such as Su-Schrieffer-Heeger (SSH) type model that has nonreciprocal hopping for every two nearest-neighbor bonds, as we have verified in the supplemental materials [84]. Our theory may be implemented, for instance, in open quantum dot [102–105], cold-atom [28, 48–50, 106–108], and monitored quantum circuit systems [109, 110].

We thank F. Alsallom, N. Astrakhantsev, M. Brzezina, J. Budich, X.-D. Cao, S.-J. Choi, C.-A. Li, L. Herviou, W. Rui, G. Tang, A. Tiwari, and O. V. Yazyev for valuable discussions. This work was supported by the European Research Council (ERC) under the European Union’s Horizon 2020 research and innovation program (ERC-StG-Neupert-757867-PARATOP) and from NCCR MARVEL funded by the SNSF. M. S. was supported by DFG through the Emmy Noether program (SE 2558/2). T. B. was supported by the Ambizione grant No. 185806 by the Swiss National Science Foundation.

*Note added in proof.* Recently, we noticed the related work [111], which focuses on the spectral winding and non-Hermitian skin effect.

- 
- [1] H. Shen, B. Zhen, and L. Fu, “Topological Band Theory for Non-Hermitian Hamiltonians”, *Phys. Rev. Lett.* **120**, 146402 (2018).
- [2] V. Kozii and L. Fu, “Non-Hermitian Topological Theory of Finite-Lifetime Quasiparticles: Prediction of Bulk Fermi Arc Due to Exceptional Point”, [arXiv:1708.05841](https://arxiv.org/abs/1708.05841).
- [3] A. A. Zyuzin and A. Y. Zyuzin, “Flat band in disorder-driven non-Hermitian Weyl semimetals”, *Phys. Rev. B* **97**, 041203 (2018).
- [4] S. Yao and Z. Wang, “Edge States and Topological Invariants of Non-Hermitian Systems”, *Phys. Rev. Lett.* **121**, 086803 (2018).
- [5] F. K. Kunst, E. Edvardsson, J. C. Budich, and E. J. Bergholtz, “Biorthogonal Bulk-Boundary Correspondence in Non-Hermitian Systems”, *Phys. Rev. Lett.* **121**, 026808 (2018).
- [6] T. E. Lee, “Anomalous edge state in a non-hermitian lattice”, *Phys. Rev. Lett.* **116**, 133903 (2016).
- [7] S. Yao, F. Song, and Z. Wang, “Non-hermitian chern bands”, *Phys. Rev. Lett.* **121**, 136802 (2018).
- [8] Z. Gong, Y. Ashida, K. Kawabata, K. Takasan, S. Higashikawa, and M. Ueda, “Topological Phases of Non-Hermitian Systems”, *Phys. Rev. X* **8**, 031079 (2018).
- [9] L. E. F. Foa Torres, “Perspective on topological states of non-Hermitian lattices”, *J. Phys. Mater.* **3**, 014002 (2020).
- [10] Y. Ashida, Z. Gong, and M. Ueda, “Non-hermitian physics”, *Adv. Phys.* **69**, 249 (2020).
- [11] M.-A. Miri and A. Alu, “Exceptional points in optics and photonics”, *Science* **363**, eaar7709 (2019).
- [12] E. J. Bergholtz, J. C. Budich, and F. K. Kunst, “Exceptional topology of non-Hermitian systems”, *Rev. Mod. Phys.* **93**, 015005 (2021).
- [13] K. Kawabata, K. Shiozaki, M. Ueda, and M. Sato, “Symmetry and Topology in Non-Hermitian Physics”, *Phys. Rev. X* **9**, 041015 (2019).
- [14] K. Zhang, Z. Yang, and C. Fang, “Correspondence between Winding Numbers and Skin Modes in Non-Hermitian Systems”, *Phys. Rev. Lett.* **125**, 126402 (2020).
- [15] N. Okuma, K. Kawabata, K. Shiozaki, and M. Sato, “Topological origin of non-hermitian skin effects”, *Phys. Rev. Lett.* **124**, 086801 (2020).
- [16] D. Leykam, K. Y. Bliokh, C. Huang, Y. D. Chong, and F. Nori, “Edge Modes, Degeneracies, and Topological Numbers in Non-Hermitian Systems”, *Phys. Rev. Lett.* **118**, 040401 (2017).
- [17] V. M. Martinez Alvarez, J. E. Barrios Vargas, and L. E. F. Foa Torres, “Non-Hermitian robust edge states in one dimension: Anomalous localization and eigenspace condensation at exceptional points”, *Phys. Rev. B* **97**, 121401 (2018).
- [18] S. Lieu, “Topological phases in the non-Hermitian Su-Schrieffer-Heeger model”, *Phys. Rev. B* **97**, 045106 (2018).
- [19] Y. Xiong, “Why does bulk boundary correspondence fail in some non-Hermitian topological models”, *J. Phys. Commun.* **2**, 035043 (2018).
- [20] T. Yoshida, R. Peters, and N. Kawakami, “Non-Hermitian perspective of the band structure in heavy-fermion systems”, *Phys. Rev. B* **98**, 035141 (2018).
- [21] W. B. Rui, M. M. Hirschmann, and A. P. Schnyder, “ $\mathcal{PT}$ -symmetric non-Hermitian Dirac semimetals”, *Phys. Rev. B* **100**, 245116 (2019).
- [22] S. Longhi, “Topological Phase Transition in non-Hermitian Quasicrystals”, *Phys. Rev. Lett.* **122**, 237601 (2019).
- [23] C. H. Lee and R. Thomale, “Anatomy of skin modes and topology in non-Hermitian systems”, *Phys. Rev. B* **99**, 201103 (2019).
- [24] K. Kawabata, T. Bessho, and M. Sato, “Classification of Exceptional Points and Non-Hermitian Topological Semimetals”, *Phys. Rev. Lett.* **123**, 066405 (2019).
- [25] T. Yoshida, R. Peters, N. Kawakami, and Y. Hatsugai, “Symmetry-protected exceptional rings in two-dimensional correlated systems with chiral symmetry”, *Phys. Rev. B* **99**, 121101 (2019).
- [26] J. Y. Lee, J. Ahn, H. Zhou, and A. Vishwanath, “Topological Correspondence between Hermitian and Non-Hermitian Systems: Anomalous Dynamics”, *Phys. Rev. Lett.* **123**, 206404 (2019).
- [27] D. S. Borgnia, A. J. Kruchkov, and R.-J. Slager, “Non-

- Hermitian Boundary Modes and Topology”, *Phys. Rev. Lett.* **124**, 056802 (2020).
- [28] L. Li, C. H. Lee, and J. Gong, “Topological Switch for Non-Hermitian Skin Effect in Cold-Atom Systems with Loss”, *Phys. Rev. Lett.* **124**, 250402 (2020).
- [29] C. C. Wojcik, X.-Q. Sun, T. Bzdušek, and S. Fan, “Homotopy characterization of non-Hermitian Hamiltonians”, *Phys. Rev. B* **101**, 205417 (2020).
- [30] M. M. Denner, A. Skurativska, F. Schindler, M. H. Fischer, R. Thomale, T. Bzdušek, and T. Neupert, “Exceptional topological insulators”, *Nature Commun.* **12**, 5681 (2021).
- [31] P. M. Vecsei, M. M. Denner, T. Neupert, and F. Schindler, “Symmetry indicators for inversion-symmetric non-Hermitian topological band structures”, *Phys. Rev. B* **103**, L201114 (2021).
- [32] F. Schindler and A. Prem, “Dislocation non-Hermitian skin effect”, *Phys. Rev. B* **104**, L161106 (2021).
- [33] J.-W. Ryu, N. Myoung, A. Go, S. Woo, S.-J. Choi, and H. C. Park, “Emergent localized states at the interface of a twofold  $\mathcal{PT}$ -symmetric lattice”, *Phys. Rev. Research* **2**, 033149 (2020).
- [34] W. Chen, Ş. K. Özdemir, G. Zhao, J. Wiersig, and L. Yang, “Exceptional points enhance sensing in an optical microcavity”, *Nature* **548**, 192 (2017).
- [35] H. Hodaie, A. U. Hassan, S. Wittek, H. Garcia-Gracia, R. El-Ganainy, D. N. Christodoulides, and M. Khajavikhan, “Enhanced sensitivity at higher-order exceptional points”, *Nature* **548**, 187 (2017).
- [36] S. Weimann, M. Kremer, Y. Plotnik, Y. Lumer, S. Nolte, K. G. Makris, M. Segev, M. C. Rechtsman, and A. Szameit, “Topologically protected bound states in photonic parity-time-symmetric crystals”, *Nature Mater.* **16**, 433 (2017).
- [37] H. Zhou, C. Peng, Y. Yoon, C. W. Hsu, K. A. Nelson, L. Fu, J. D. Joannopoulos, M. Soljačić, and B. Zhen, “Observation of bulk Fermi arc and polarization half charge from paired exceptional points”, *Science* **359**, 1009 (2018).
- [38] H. Zhao, X. Qiao, T. Wu, B. Midya, S. Longhi, and L. Feng, “Non-Hermitian topological light steering”, *Science* **365**, 1163 (2019).
- [39] A. Cerjan, S. Huang, M. Wang, K. P. Chen, Y. Chong, and M. C. Rechtsman, “Experimental realization of a Weyl exceptional ring”, *Nature Photonics* **13**, 623 (2019).
- [40] T. Helbig, T. Hofmann, S. Imhof, M. Abdelghany, T. Kiessling, L. Molenkamp, C. Lee, A. Szameit, M. Greiter, and R. Thomale, “Generalized bulk-boundary correspondence in non-Hermitian topoelectrical circuits”, *Nature Phys.* **16**, 747 (2020).
- [41] S. Weidemann, M. Kremer, T. Helbig, T. Hofmann, A. Stegmaier, M. Greiter, R. Thomale, and A. Szameit, “Topological funneling of light”, *Science* **368**, 311 (2020).
- [42] L. Xiao, T. Deng, K. Wang, G. Zhu, Z. Wang, W. Yi, and P. Xue, “Non-Hermitian bulk-boundary correspondence in quantum dynamics”, *Nature Phys.* **16**, 761 (2020).
- [43] A. Ghatak, M. Brandenbourger, J. van Wezel, and C. Coulais, “Observation of non-Hermitian topology and its bulk-edge correspondence in an active mechanical metamaterial”, *Proc. Nat. Acad. Sci.* **117**, 29561 (2020).
- [44] W. Zhang, X. Ouyang, X. Huang, X. Wang, H. Zhang, Y. Yu, X. Chang, Y. Liu, D.-L. Deng, and L.-M. Duan, “Observation of Non-Hermitian Topology with Nonunitary Dynamics of Solid-State Spins”, *Phys. Rev. Lett.* **127**, 090501 (2021).
- [45] S. Xia, D. Kaltsas, D. Song, I. Komis, J. Xu, A. Szameit, H. Buljan, K. G. Makris, and Z. Chen, “Nonlinear tuning of  $\mathcal{PT}$  symmetry and non-Hermitian topological states”, *Science* **372**, 72 (2021).
- [46] R. Su, E. Estrecho, D. Biegańska, Y. Huang, M. Wurdack, M. Pieczarka, A. G. Truscott, T. C. H. Liew, E. A. Ostrovskaya, and Q. Xiong, “Direct measurement of a non-Hermitian topological invariant in a hybrid light-matter system”, *Sci. Adv.* **7**, eabj8905 (2021).
- [47] K. Wang, A. Dutt, K. Y. Yang, C. C. Wojcik, J. Vucković, and S. Fan, “Generating arbitrary topological windings of a non-Hermitian band”, *Science* **371**, 1240 (2021).
- [48] W. Guo, T. Chen, D. Xie, T. S. Deng, B. Gadway, W. Yi, and B. Yan, “Tunable Nonreciprocal Quantum Transport through a Dissipative Aharonov-Bohm Ring in Ultracold Atoms”, *Phys. Rev. Lett.* **124**, 070402 (2020).
- [49] Q. Liang, D. Xie, Z. Dong, H. Li, Z. Gadway, W. Yi, and B. Yan, “Observation of Non-Hermitian Skin Effect and Topology in Ultracold Atoms”, [arXiv:2201.09478](https://arxiv.org/abs/2201.09478).
- [50] Z. Ren, D. Liu, E. Zhao, C. He, K. K. Pak, J. Li, and G. B. Jo, “Chiral control of quantum states in non-Hermitian spin-orbit-coupled fermions”, *Nature Phys.* **16**, 1-5 (2022).
- [51] F. Haldane, “Luttinger liquid theory of one-dimensional quantum fluids. I. Properties of the Luttinger model and their extension to the general 1D interacting spinless Fermi gas”, *J. Phys. C: Solid State Phys.* **14**, 2585 (1981).
- [52] T. Giamarchi, *Quantum physics in one dimension*, Vol. 121 (Clarendon press, 2003).
- [53] E. Fradkin, *Field theories of condensed matter physics* (Cambridge University Press, 2013).
- [54] M. Nakagawa, N. Kawakami, and M. Ueda, “Non-Hermitian Kondo Effect in Ultracold Alkaline-Earth Atoms”, *Phys. Rev. Lett.* **121**, 203001 (2018).
- [55] T. Yoshida, K. Kudo, and Y. Hatsugai, “Non-Hermitian fractional quantum Hall states”, *Sci. Rep.* **9**, 16895 (2019).
- [56] R. Hamazaki, K. Kawabata, and M. Ueda, “Non-Hermitian Many-Body Localization”, *Phys. Rev. Lett.* **123**, 090603 (2019).
- [57] G.-Q. Zhang, D.-W. Zhang, Z. Li, Z. D. Wang, and S.-L. Zhu, “Statistically related many-body localization in the one-dimensional anyon Hubbard model”, *Phys. Rev. B* **102**, 054204 (2020).
- [58] L.-J. Zhai, S. Yin, and G.-Y. Huang, “Many-body localization in a non-Hermitian quasiperiodic system”, *Phys. Rev. B* **102**, 064206 (2020).
- [59] N. Fayard, L. Henriot, A. Asenjo-Garcia, and D. E. Chang, “Many-body localization in waveguide quantum electrodynamics”, *Phys. Rev. Research* **3**, 033233 (2021).
- [60] K. Yamamoto, M. Nakagawa, K. Adachi, K. Takasan, M. Ueda, and N. Kawakami, “Theory of Non-Hermitian Fermionic Superfluidity with a Complex-Valued Interaction”, *Phys. Rev. Lett.* **123**, 123601 (2019).
- [61] E. Lee, H. Lee, and B.-J. Yang, “Many-body approach to non-Hermitian physics in fermionic systems”, *Phys.*

- Rev. B **101**, 121109 (2020).
- [62] S. Mu, C. H. Lee, L. Li, and J. Gong, “Emergent Fermi surface in a many-body non-Hermitian fermionic chain”, *Phys. Rev. B* **102**, 081115 (2020).
- [63] D.-W. Zhang, Y.-L. Chen, G.-Q. Zhang, L.-J. Lang, Z. Li, and S.-L. Zhu, “Skin superfluid, topological Mott insulators, and asymmetric dynamics in an interacting non-Hermitian Aubry-André-Harper model”, *Phys. Rev. B* **101**, 235150 (2020).
- [64] T. Liu, J. J. He, T. Yoshida, Z.-L. Xiang, and F. Nori, “Non-Hermitian topological Mott insulators in one-dimensional fermionic superlattices”, *Phys. Rev. B* **102**, 235151 (2020).
- [65] A. Panda and S. Banerjee, “Entanglement in nonequilibrium steady states and many-body localization breakdown in a current-driven system”, *Phys. Rev. B* **101**, 184201 (2020).
- [66] N. Okuma and M. Sato, “Non-Hermitian Skin Effects in Hermitian Correlated or Disordered Systems: Quantities Sensitive or Insensitive to Boundary Effects and Pseudo-Quantum-Number”, *Phys. Rev. Lett.* **126**, 176601 (2021).
- [67] T. Yoshida, “Real-space dynamical mean field theory study of non-Hermitian skin effect for correlated systems: Analysis based on pseudospectrum”, *Phys. Rev. B* **103**, 125145 (2021).
- [68] K. Cao, Q. Du, X.-R. Wang, and S.-P. Kou, “Physics of Many-body Nonreciprocal Model: Quantum system with Maxwell’s Pressure Demon”, [arXiv:2109.03690](https://arxiv.org/abs/2109.03690).
- [69] F. Alsallom, L. Herviou, O. V. Yazyev, and M. Brzezińska, “Fate of the non-Hermitian skin effect in many-body fermionic systems”, [arXiv:2110.13164](https://arxiv.org/abs/2110.13164).
- [70] A. Y. Guo, S. Lieu, M. C. Tran, and A. V. Gorshkov, “Clustering of steady-state correlations in open systems with long-range interactions”, [arXiv:2110.15368](https://arxiv.org/abs/2110.15368).
- [71] Y.-G. Liu, L. Xu, and Z. Li, “Quantum phase transition in a non-Hermitian XY spin chain with global complex transverse field”, *J. Phys. Condens. Matter* **33**, 295401 (2021).
- [72] B. Dóra and C. P. Moca, “Quantum Quench in  $\mathcal{PT}$ -Symmetric Luttinger Liquid”, *Phys. Rev. Lett.* **124**, 136802 (2020).
- [73] W. Xi, Z.-H. Zhang, Z.-C. Gu, and W.-Q. Chen, “Classification of topological phases in one dimensional interacting non-Hermitian systems and emergent unitarity”, *Sci. Bull.* **66**, 1731 (2021).
- [74] L. Pan, X. Wang, X. Cui, and S. Chen, “Interaction-induced dynamical  $\mathcal{PT}$ -symmetry breaking in dissipative Fermi-Hubbard models”, *Phys. Rev. A* **102**, 023306 (2020).
- [75] Z. Xu and S. Chen, “Topological Bose-Mott insulators in one-dimensional non-Hermitian superlattices”, *Phys. Rev. B* **102**, 035153 (2020).
- [76] T. Hyart and J. L. Lado, “Non-Hermitian many-body topological excitations in interacting quantum dots”, *Phys. Rev. Research* **4**, L012006 (2022).
- [77] L. Crippa, J. C. Budich, and G. Sangiovanni, “Fourth-order exceptional points in correlated quantum many-body systems”, *Phys. Rev. B* **104**, L121109 (2021).
- [78] Z. Wang, L.-J. Lang, and L. He, “Emergent Mott insulators at non-integer fillings and non-Hermitian conservation laws in an interacting bosonic chain with nonreciprocal hoppings”, [arXiv:2111.02911](https://arxiv.org/abs/2111.02911).
- [79] A. Banerjee, S.-S. Hegde, A. Agarwala, and A. Narayan, “Chiral metals and entrapped insulators in a one-dimensional topological non-Hermitian system”, [arXiv:2111.02223](https://arxiv.org/abs/2111.02223).
- [80] N. Hatano and D. R. Nelson, “Localization Transitions in Non-Hermitian Quantum Mechanics”, *Phys. Rev. Lett.* **77**, 570 (1996).
- [81] Here, we are mainly interested in the low- $\text{Re}(E)$  regime of the spectrum. As in Hermitian systems, we refer the ground state to the state with the lowest  $\text{Re}(E)$ , and rank the excited states by their  $\text{Re}(E)$  from low to high.
- [82] K. Zhang, Z. Yang, and C. Fang, “Universal non-Hermitian skin effect in two and higher dimensions”, [arXiv:2102.05059](https://arxiv.org/abs/2102.05059).
- [83] T. Fukui and N. Kawakami, “Breakdown of the Mott insulator: Exact solution of an asymmetric Hubbard model”, *Phys. Rev. B* **58**, 16051 (1998).
- [84] See the Supplemental Material (SM) for details, which includes Refs. [12, 14, 15, 90, 99–101].
- [85] Such a nonreciprocal hopping can be generated in cold-atom systems via synthetic magnetic flux and laser-induced loss, see e.g., Refs. [48, 49].
- [86] We note that for  $\gamma < 0.03$ , we cannot extrapolate  $U_{\text{TD}}$  accurately with the exact-diagonalization results even up to the largest system size ( $L = 30$ ) that we can achieve in numerics. However, we observe that  $U_{\text{TD}}$  approaches  $2t$  as  $\gamma \rightarrow 0$ .
- [87] I. Affleck and E. H. Lieb, “A proof of part of Haldane’s conjecture on spin chains”, in *Condensed Matter Physics and Exactly Soluble Models* (Springer, 1986) pp. 235–247.
- [88] M. Dalmonte, J. Carrasquilla, L. Taddia, E. Ercolessi, and M. Rigol, “Gap scaling at Berezinskii-Kosterlitz-Thouless quantum critical points in one-dimensional Hubbard and Heisenberg models”, *Phys. Rev. B* **91**, 165136 (2015).
- [89] In the Hermitian limit, Eq. (1) can be mapped to the XXZ model by Jordan-Wigner transformation.
- [90] N. Byers and C. N. Yang, “Theoretical considerations concerning quantized magnetic flux in superconducting cylinders”, *Phys. Rev. Lett.* **7**, 46 (1961).
- [91] We note that a small magnetic flux  $\phi$  will break the  $\mathcal{PT}$  symmetry and generate a small imaginary free energy. Thus, the derivative of the free energy with respect to  $\phi$  can be finite, leading to an imaginary persistent current. Imaginary persistent currents in non-Hermitian systems have been reported previously, see e.g., [80, 96, 97]. However, they all focused on single-particle systems without interactions. A persistent current was also obtained within a field theoretical calculation in Ref. [98], which, in contrast to the current obtained in our tight-binding calculation, is real and quantized. Reconciling these results is an interesting question for future work.
- [92] H.-F. Cheung, Y. Gefen, E. K. Riedel, and W.-H. Shih, “Persistent currents in small one-dimensional metal rings”, *Phys. Rev. B* **37**, 6050 (1988).
- [93] Namely, the number of bonds connecting two simultaneously occupied adjacent sites.
- [94] For small  $U < \Xi_R$ , nontrivial winding numbers and the resulting many-body skin effect can also be found, as we have shown in Fig. S4 in the SM. However, these winding numbers may change as  $U$  changes. The exact relation between these many-body winding numbers and a physical observable remains an open question.
- [95] In many-body fermionic systems, the localization length

- of eigen wavefunctions in the presence of open boundaries depends on the particle number  $N$ . When the system is close to half-filling and for small  $\gamma$ , the localization length is comparable to  $L$ . In this case, it is hard to observe the localization behavior, as mentioned in Ref. [61]. However, when the localization length is much smaller than  $L$  (i.e., in the case with finite  $N$  and large  $L$  which we are considering), one can observe clearly the localization of all many-body wavefunctions to an open boundary. This localization behavior becomes constant for increasing  $L$  (but fixed  $N$ ), similar to the non-Hermitian skin effect in single-particle systems.
- [96] N. Hatano and D. R. Nelson, “Vortex pinning and non-Hermitian quantum mechanics”, *Phys. Rev. B* **56**, 8651 (1997).
- [97] Q. Li, J.-J. Liu, and Y.-T. Zhang, “Non-Hermitian Aharonov-Bohm effect in the quantum ring”, *Phys. Rev. B* **103**, 035415 (2021).
- [98] K. Kawabata, K. Shiozaki, and S. Ryu, “Topological Field Theory of Non-Hermitian Systems”, *Phys. Rev. Lett.* **126**, 216405 (2021).
- [99] M. H. Kalthoff, D. M. Kennes, and M. A. Sentef, “Floquet-engineered light-cone spreading of correlations in a driven quantum chain”, *Phys. Rev. B* **100**, 165125 (2019).
- [100] G. Lindblad, “On the generators of quantum dynamical semigroups”, *Commun. Math. Phys.* **48**, 119 (1976).
- [101] A. J Daley, “Quantum trajectories and open many-body quantum systems”, *Adv. Phys.* **63**, 77 (2014).
- [102] D. K. Ferry, R. Akis, A. M. Burke, I. Knezevic, R. Brunner, R. Meisels, F. Kuchar, and J. P. Bird, “Open quantum dots: Physics of the non-Hermitian Hamiltonian”, *Fortschr. Phys.* **61**, 291 (2013).
- [103] L. L. Zhang, G. H. Zhan, D. Q. Yu, and W. J. Gong, “Transport through a non-Hermitian parallel double-quantum-dot structure in the presence of interdot Coulomb interaction”, *Fortschr. Phys.* **113**, 558 (2018).
- [104] D. M. Zajac, T. M. Hazard, X. Mi, E. Nielsen, and J. R. Petta, “Scalable Gate Architecture for a One-Dimensional Array of Semiconductor Spin Qubits”, *Phys. Rev. Applied* **6**, 054013 (2016).
- [105] T. Hensgens, T. Fujita, L. Janssen, X. Li, C. J. Van Diepen, C. Reichl, W. Wegscheider, S. Das Sarma, and J. R. Petta, “Quantum simulation of a Fermi-Hubbard model using a semiconductor quantum dot array”, *Nature* **548**, 70-73 (2017).
- [106] C. Chin, R. Grimm, P. Julienne, and E. Tiesinga, “Feshbach resonances in ultracold gases”, *Rev. Mod. Phys.* **82**, 1225 (2010).
- [107] L. Zhou, D. Liu, H. Li, W. Yi, and X. L. Cui, “Engineering Non-Hermitian Skin Effect with Band Topology in Ultracold Gases”, [arXiv:2111.04196](https://arxiv.org/abs/2111.04196).
- [108] S. Guo, C. Dong, F. Zhang, J. Hu, and Z. Yang, “Theoretical Prediction of Non-Hermitian Skin Effect in Ultracold Atom Systems”, [arXiv:2111.04220](https://arxiv.org/abs/2111.04220).
- [109] G. Kells, D. Meidan, and A. Romito, “Topological transitions with continuously monitored free fermions”, [arXiv:2112.09787](https://arxiv.org/abs/2112.09787).
- [110] C. Fleckenstein, A. Zorzato, D. Varjas, E. J. Bergholtz, J. H. Bardarson, and A. Tiwari, “Non-Hermitian topology in monitored quantum circuits”, [arXiv:2201.05341](https://arxiv.org/abs/2201.05341).
- [111] K. Kawabata, K. Shiozaki, and S. Ryu, “Many-body topology of non-Hermitian systems”, *Phys. Rev. B* **105**, 165137 (2022).



In this Supplemental Material, we present the analysis of the system symmetries (Sec. I), Pauli exclusion principle (Sec. II), dimensions of the many-body spectrum (Sec. III), more discussions of critical interaction strength (Sec. IV), density-density correlation (Sec. V), free energy and persistent current (Sec. VI), spectral winding numbers and charge-density profiles (Sec. VII), other complementary half-filled cases (Sec. VIII), and the non-Hermitian SSH-type model (Sec. IX).

### Appendix I: $\mathcal{PT}$ and particle-hole symmetries

For general twisted periodic boundary conditions (PBC) characterized by a twist boundary angle  $\phi$ , the Hamiltonian reads

$$\hat{H} = \sum_{\ell=1}^{L-1} [(t + \gamma)\hat{c}_{\ell}^{\dagger}\hat{c}_{\ell+1} + (t - \gamma)\hat{c}_{\ell+1}^{\dagger}\hat{c}_{\ell} + U\hat{n}_{\ell}\hat{n}_{\ell+1}] + e^{i\phi}(t + \gamma)\hat{c}_L^{\dagger}\hat{c}_1 + e^{-i\phi}(t - \gamma)\hat{c}_1^{\dagger}\hat{c}_L + U\hat{n}_L\hat{n}_1, \quad (\text{I1})$$

Particularly,  $\phi = 0$  and  $\pi$  correspond to PBC and anti-PBC, respectively. We define the  $\mathcal{PT}$  symmetry operation as

$$\mathcal{PT}\hat{c}_{\ell}(\mathcal{PT})^{-1} = \hat{c}_{L+1-\ell}, \quad \mathcal{PT}i(\mathcal{PT})^{-1} = -i. \quad (\text{I2})$$

Acting with  $\mathcal{PT}$  on  $\hat{H}$ , we find

$$\begin{aligned} & \mathcal{PT}\hat{H}(\mathcal{PT})^{-1} \\ &= \mathcal{PT} \left\{ \sum_{\ell=1}^{L-1} [(t + \gamma)\hat{c}_{\ell}^{\dagger}\hat{c}_{\ell+1} + (t - \gamma)\hat{c}_{\ell+1}^{\dagger}\hat{c}_{\ell} + U\hat{n}_{\ell}\hat{n}_{\ell+1}] + e^{i\phi}(t + \gamma)\hat{c}_L^{\dagger}\hat{c}_1 + e^{-i\phi}(t - \gamma)\hat{c}_1^{\dagger}\hat{c}_L + U\hat{n}_L\hat{n}_1 \right\} (\mathcal{PT})^{-1} \\ &= \sum_{\ell=1}^{L-1} [(t + \gamma)\hat{c}_{L+1-\ell}^{\dagger}\hat{c}_{L-\ell} + (t - \gamma)\hat{c}_{L-\ell}^{\dagger}\hat{c}_{L+1-\ell} + U\hat{n}_{L+1-\ell}\hat{n}_{L-\ell}] + e^{-i\phi}(t + \gamma)\hat{c}_1^{\dagger}\hat{c}_L + e^{i\phi}(t - \gamma)\hat{c}_L^{\dagger}\hat{c}_1 + U\hat{n}_1\hat{n}_L \\ &= \sum_{j=1}^{L-1} [(t + \gamma)\hat{c}_{j+1}^{\dagger}\hat{c}_j + (t - \gamma)\hat{c}_j^{\dagger}\hat{c}_{j+1} + U\hat{n}_{j+1}\hat{n}_j] + [e^{i\phi}(t + \gamma)\hat{c}_L^{\dagger}\hat{c}_1 + e^{-i\phi}(t - \gamma)\hat{c}_1^{\dagger}\hat{c}_L]^{\dagger} + U\hat{n}_1\hat{n}_L. \end{aligned} \quad (\text{I3})$$

In the last line, we have replaced  $j = L - \ell$ . For PBC and anti-PBC, it follows that

$$\mathcal{PT}\hat{H}(\mathcal{PT})^{-1} = \hat{H}^{\dagger}. \quad (\text{I4})$$

This relation indicates that the eigenenergies of  $\hat{H}$  must either be real or come in complex-conjugate pairs.

To see the particle-hole symmetry explicitly, we divide the lattices into two sublattices  $A$  and  $B$  of even and odd sites. We perform the transformation  $\hat{c}_{\ell}^{\dagger} \rightarrow \hat{c}_{\ell}$  and  $\hat{c}_{\ell} \rightarrow \hat{c}_{\ell}^{\dagger}$  on sublattice  $A$  while  $\hat{c}_{\ell}^{\dagger} \rightarrow -\hat{c}_{\ell}$  and  $\hat{c}_{\ell} \rightarrow -\hat{c}_{\ell}^{\dagger}$  on sublattice  $B$ . Accordingly, the transformation for the occupation number operators reads  $\hat{n}_{\ell} \rightarrow 1 - \hat{n}_{\ell}$ . Then, it is clear to see that the transformed Hamiltonian takes the same form up to a constant energy shift.

### Appendix II: Pauli exclusion principle

In this work, we consider the interacting Hatano-Nelson model which can be written in the basis of conventional fermionic operators  $\hat{c}_{\ell}^{\dagger}$  and  $\hat{c}_{\ell}$  as

$$\hat{H} = \sum_{\ell=1}^L [(t + \gamma)\hat{c}_{\ell}^{\dagger}\hat{c}_{\ell+1} + (t - \gamma)\hat{c}_{\ell+1}^{\dagger}\hat{c}_{\ell} + U\hat{n}_{\ell}\hat{n}_{\ell+1}]. \quad (\text{II1})$$

The fermionic operators  $\hat{c}_{\ell}^{\dagger}$  and  $\hat{c}_{\ell}$  follow the anticommutation relations

$$\{\hat{c}_{\ell}^{\dagger}, \hat{c}_j\} = \delta_{\ell,j}, \quad \{\hat{c}_{\ell}, \hat{c}_j\} = 0. \quad (\text{II2})$$

With these relations, we find that the number operator  $\hat{n}_j \equiv \hat{c}_j^{\dagger}\hat{c}_j$  at site  $j$  follows the relation

$$\hat{n}_j^2 = \hat{c}_j^{\dagger}\hat{c}_j\hat{c}_j^{\dagger}\hat{c}_j = \hat{c}_j^{\dagger}(1 - \hat{c}_j^{\dagger}\hat{c}_j)\hat{c}_j = \hat{c}_j^{\dagger}\hat{c}_j = \hat{n}_j, \quad (\text{II3})$$

which gives  $\hat{n}_j = 0$  or 1. This means that an arbitrary site  $j$  is at most occupied by one electron, which is the Pauli exclusion principle considered in this work.

The single-particle eigenstates also follow the Pauli exclusion principle. To illustrate this, we rewrite the single-particle Hamiltonian (with  $U = 0$ ) as

$$\hat{H} = \sum_n E_n |R_n\rangle \langle L_n|, \quad (\text{II4})$$

where  $|L_n\rangle$  and  $|R_n\rangle$  are the left and right eigenstates of  $\hat{H}$ , satisfying  $\hat{H}|R_n\rangle = E_n|R_n\rangle$  and  $\hat{H}^\dagger|L_n\rangle = E_n^*|L_n\rangle$ , respectively. The left and right eigenstates have the biorthogonal relations  $\langle L_m|R_n\rangle = \delta_{m,n}$ . If we define  $d_{n,R}^\dagger$  ( $d_{n,L}^\dagger$ ) as the creation operator related to the eigenstate  $|R_n\rangle$  ( $|L_n\rangle$ ),

$$d_{n,R}^\dagger = \sum_\ell \langle \ell|R_n\rangle c_\ell^\dagger, \quad (\text{II5})$$

then we find that these operators have the following modified anticommutation relations

$$\begin{aligned} \{d_{m,R}^\dagger, d_{n,L}\} &= \delta_{m,n}, \\ \{d_{m,R}^\dagger, d_{n,R}^\dagger\} &= 0, \\ \{d_{m,R}^\dagger, d_{n,R}\} &= \langle R_n|R_m\rangle. \end{aligned} \quad (\text{II6})$$

Note that for non-Hermitian system, not all the eigenstates  $|R_m\rangle$  are orthogonal, i.e.,  $\langle R_n|R_m\rangle$  could be finite even for  $m \neq n$ . Using the modified anticommutation relations in Eq. (II6), we find that the number operator  $\hat{\mathfrak{N}}_m \equiv d_{m,R}^\dagger d_{m,R}$  for the eigenstate  $|R_m\rangle$  follows

$$\hat{\mathfrak{N}}_m^2 = d_{m,R}^\dagger \left( \langle R_m|R_m\rangle - d_{m,R}^\dagger d_{m,R} \right) d_{m,R} = \langle R_m|R_m\rangle \hat{\mathfrak{N}}_m. \quad (\text{II7})$$

Thus,  $\hat{\mathfrak{N}}_m$  can only have the eigenvalues 0 and  $\langle R_m|R_m\rangle$ , where the latter can be different from 1 (in particular larger). Similar results can be obtained for the left eigenstates. These results show that the eigenstates also obey the Pauli exclusion principle, i.e., a fermionic state can be occupied at most by one particle simultaneously.

### Appendix III: Dimension of the many-body spectrum

The extent of the spectrum at  $U = 0$  on the real and imaginary axes can be written as

$$\Xi_{\text{R}} \approx t\alpha_{\{N,L\}} \text{ and } \Xi_{\text{I}} \approx \gamma\alpha_{\{N,L\}}, \quad (\text{III1})$$

where  $\kappa$  are integers,  $n_{\text{cl}} \equiv \min(N, L - N)$  and

$$\alpha_{\{N,L\}} = 2 \sum_{|\kappa| \leq n_{\text{cl}}/2} \cos(2\pi\kappa/L). \quad (\text{III2})$$

For  $n_{\text{cl}} \gg 1$ , we transform the summation in Eq. (III2) to an integral and obtain

$$\alpha_{\{N,L\}} = \frac{2L}{\pi} \sin\left(\frac{n_{\text{cl}}\pi}{L}\right). \quad (\text{III3})$$

At half-filling,  $n_{\text{cl}} = L/2$ . Thus,  $\alpha_{\{N,L\}}$  simplifies to

$$\alpha_{\{N,L\}} = \frac{2L}{\pi}. \quad (\text{III4})$$

### Appendix IV: Critical interaction strength in the thermodynamic limit

The dependence of  $U_c$  on  $L$  follows a power-law scaling, as shown in Fig. S1(a). The circle dots are numerical results obtained by exact diagonalization while the curves are the fitting with the power-law relation, Eq. (2) in the main text. The extrapolated  $U_c = U_{\text{TD}}$  in the TDL is shown by the red line in Fig. 1(c) of the main text. The fitting parameters  $\alpha$  and  $\beta$  depend explicitly on  $\gamma$ , as shown in Fig. S1(b).

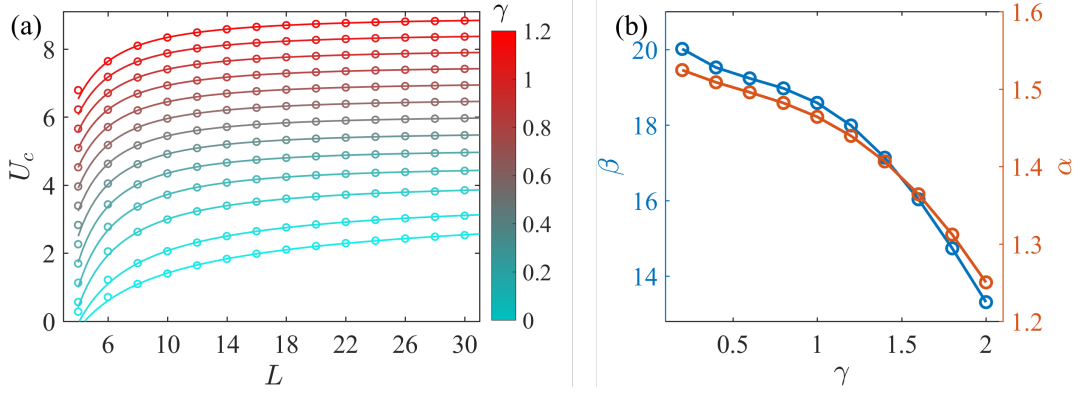


Fig. S1. (a) Critical interaction strength  $U_c$  as a function of  $L$  for different nonreciprocity  $\gamma$ . The color changes from cyan to red when  $\gamma$  increases from 0 to  $1.2t$ . The circle dots are exact diagonalization results and the curves are the fitting with the power-law relation, Eq. (2), in the main text. (b) Extrapolated index  $\alpha$  (right orange) and decaying strength  $\beta$  (left blue) as functions of  $\gamma$ .

### Appendix V: Density-density correlation function

To characterize the phase diagram, we compute the density-density correlation function by [99]

$$\begin{aligned} \mathcal{C}_\ell &= \langle (\hat{n}_0 - 1/2)(\hat{n}_\ell - 1/2) \rangle \\ &= \frac{\sum_j \langle j | (\hat{n}_0 - 1/2)(\hat{n}_\ell - 1/2) e^{-\beta E_j} | j \rangle}{\mathcal{Z}}, \end{aligned} \quad (\text{V1})$$

where  $|j\rangle$  are the right eigenstates of the many-body Hamiltonian with eigenvalues  $E_j$ ,  $\mathcal{Z}$  is the partition function given by Eq. (VI2). For concreteness, we consider the long-range correlation function with  $\ell = L/2$  and at low temperatures  $1/\beta = k_B T \ll t$ . In the low-temperature limit  $\beta \rightarrow \infty$ , Eq. (V1) describes the density-density correlation of the ground state. The correlation function as a function of interaction strength  $U$  for increasing  $L$  is shown in Fig. S2. At  $U = 0$ , we find  $\mathcal{C}_{L/2} = 0$ . When increasing  $U$ ,  $|\mathcal{C}_{L/2}|$  increases slowly in the small  $U$  regime but rapidly around  $U = U_c$ . In the large  $U$  regime,  $|\mathcal{C}_{L/2}|$  saturates slowly to a universal value 0.25. For larger systems, these features are more pronounced. In the TDL, we can expect  $|\mathcal{C}_{L/2}|$  to suddenly jump from zero to the universal value 0.25 at the transition, as sketched by the red dotted curve in Fig. S2(a). A similar behavior of  $|\mathcal{C}_{L/2}|$  happens for  $\gamma = 0$  but with the rapid increment around a smaller  $U$ , as shown in Fig. S2(b). Finally, we note that for odd  $L/2$ , we have always  $\mathcal{C}_{L/2} \geq 0$ , while for even  $L/2$ , we have always  $\mathcal{C}_{L/2} \leq 0$ . This reflects the fact that the ground state of the system is likely to have staggered charge-density distribution, namely, different charge densities at odd and even lattice sites.

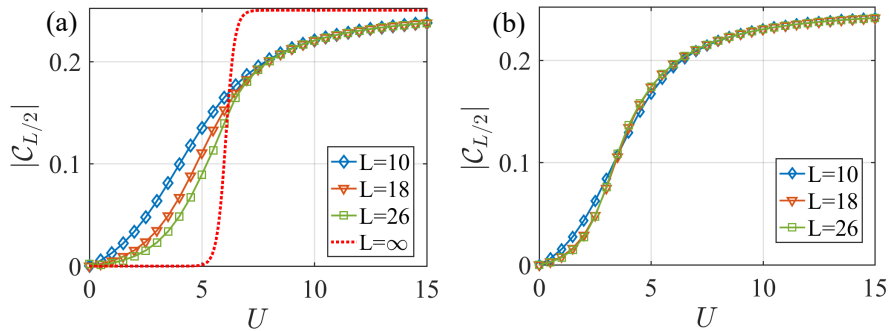


Fig. S2. (a) Density-density correlation function as a function of  $U$  for different  $L$ . The red dotted curve sketches the result in the TDL. Other parameters are  $\gamma = 0.6t$  and  $k_B T = 0.1t$ . (b) is the same as (a) but for the Hermitian limit  $\gamma = 0$ .

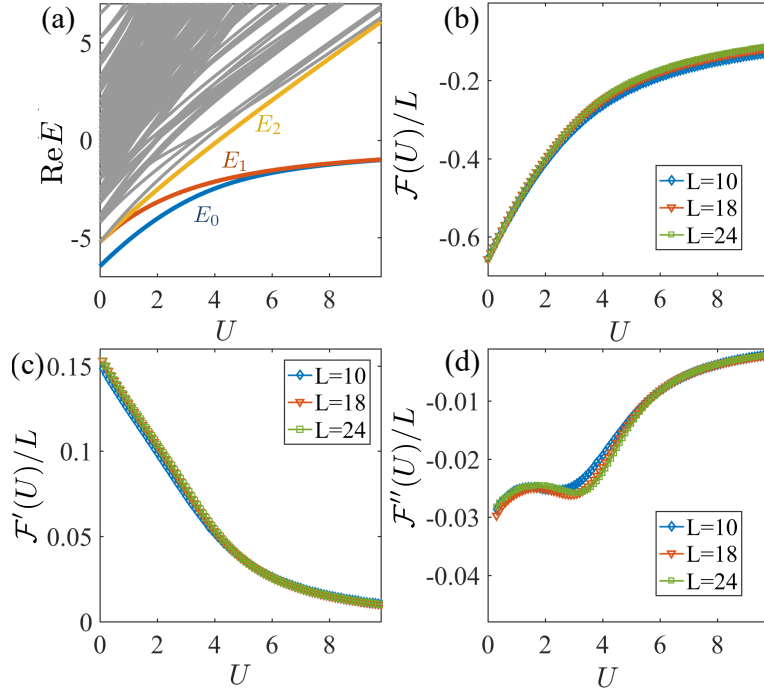


Fig. S3. (a) Real part of the low- $\text{Re}(E)$  spectrum as a function of  $U$ . We take  $L = 10$  for illustration. (b) Free energy  $\mathcal{F}(U)$ , its first (c)  $\mathcal{F}'(U)$  and second (d) derivative  $\mathcal{F}''(U)$  as functions of  $U$ . In contrast to the case with finite  $\gamma \neq 0$ ,  $\mathcal{F}$  and its derivatives change smoothly when increasing  $U$ .  $\gamma = 0$  and other parameters are the same as Fig. 3 in the main text.

### Appendix VI: Free energy and persistent current

The free energy  $\mathcal{F}$  of the interacting system at temperature  $T$  is given by

$$\mathcal{F} = -\frac{1}{\beta} \log \mathcal{Z}, \quad (\text{VI1})$$

where  $\beta = 1/k_{\text{B}}T$  with  $k_{\text{B}}$  being the Boltzmann constant, and  $\mathcal{Z}$  is the partition function

$$\mathcal{Z} = \sum_j e^{-\beta E_j}. \quad (\text{VI2})$$

The sum in Eq. (VI2) runs over all eigenenergies. In the Hermitian limit  $\gamma = 0$ , all eigenenergies change smoothly with increasing  $U$  [Fig. S3(a)]. Consequently,  $\mathcal{F}$  and its derivative also change smoothly, as shown in Figs. S3(b–d).

The application of a magnetic flux  $\phi$  thread through the ring changes the eigenenergies and hence  $\mathcal{F}$  periodically. The persistent current along the ring can be found as the derivative of  $\mathcal{F}$  with respect to  $\phi$  [90], i.e.,

$$I_{\text{p}} = -\frac{e}{\hbar} \frac{\partial \mathcal{F}}{\partial \phi}, \quad (\text{VI3})$$

where  $e$  is the elementary charge and  $\hbar$  the reduced Planck constant.

At zero temperature, the free energy is equal to the ground-state energy, i.e.,  $\mathcal{F} = E_0$ . In the absence of interactions, the ground-state energy can be found as

$$E_0(\phi) = -2 \sum_{|\kappa| \leq L/4} \left[ t \cos\left(\frac{2\pi\kappa}{L} + \frac{\phi}{L}\right) + i\gamma \sin\left(\frac{2\pi\kappa}{L} + \frac{\phi}{L}\right) \right], \quad (\text{VI4})$$

where  $\kappa$  are integers. For  $L \gg 1$ , we approximate the summation in Eq. (VI4) as an integral and obtain

$$\begin{aligned} E_0(\phi) &= -\frac{L}{\pi} \int_{-\pi/2}^{\pi/2} dx \left[ t \cos(x) \cos\left(\frac{\phi}{L}\right) - t \sin(x) \sin\left(\frac{\phi}{L}\right) + i\gamma \sin(x) \cos\left(\frac{\phi}{L}\right) + i\gamma \cos(x) \sin\left(\frac{\phi}{L}\right) \right] \\ &= -\frac{2L}{\pi} \left[ t \cos\left(\frac{\phi}{L}\right) + i\gamma \sin\left(\frac{\phi}{L}\right) \right]. \end{aligned} \quad (\text{VI5})$$

Plugging  $\mathcal{F} = E_0$  into Eq. (VI3), we find

$$I_p = \frac{2e}{\hbar\pi} \left[ -t \sin\left(\frac{\phi}{L}\right) + i\gamma \cos\left(\frac{\phi}{L}\right) \right]. \quad (\text{VI6})$$

At zero flux  $\phi = 0$ , the persistent current is given by

$$I_p = i \frac{2e}{\hbar} \frac{\gamma}{\pi}. \quad (\text{VI7})$$

### Appendix VII: Nontrivial winding numbers and charge density profiles of the many-body eigenstates

At  $U = 0$ , the flow of the eigenenergies as varying the twist boundary angle  $\phi$  in a period  $[0, 2\pi)$ , and charge-density profiles of all many-body sates are shown in Fig. S4. In the strong interaction regime, the flow of the eigenenergies and charge-density profiles of the many-body eigenstates associated with the spectral clusters (i.e., with the energies close to the respective cluster energy centers) are shown in Fig. S5. Clearly, all the eigenenergies wind around the corresponding energy centers when  $\phi$  increases from 0 to  $2\pi$ . Correspondingly, the charge densities of the many-body eigenstates, which are evenly distributed in the system under PBC, tend to localize to an open boundary. We note that the winding numbers defined by Eq. (3) in the main text are applicable to finite-size systems. Due to the finite-size effect, all eigenenergies are away from the energy centers of clusters, provided that  $U$  is finite. Thus, the clusters have well-defined point gaps in finite-size systems. In the  $L \rightarrow \infty$  limit but with fixed  $N$ , each clusters has at least one continuous orbit surrounding their energy centers. Nontrivial topological invariants can be defined as the winding numbers along these orbits.

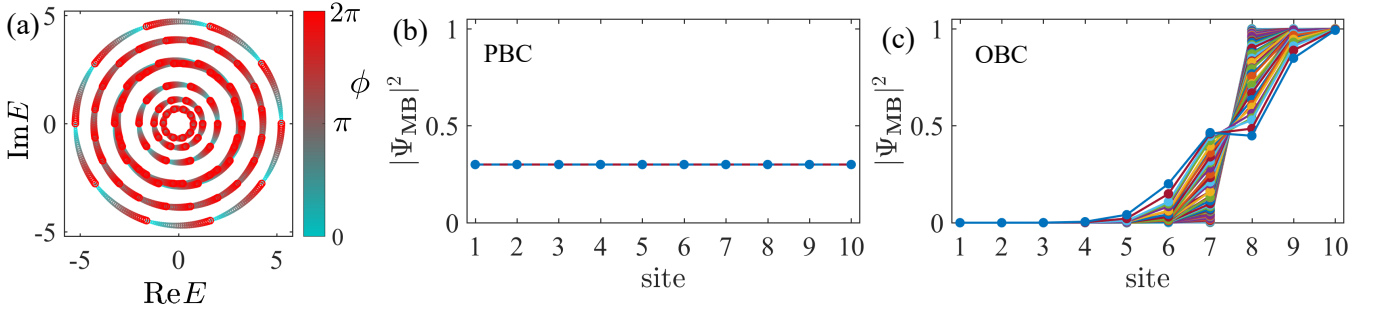


Fig. S4. (a) Movement of the eigenenergies at  $U = 0$  as the twist boundary angle  $\phi$  increases from 0 (cyan) to  $2\pi$  (red). All eigenenergies wind around  $E = 0$  in one direction. The spectral winding number for the spectrum is found as  $\nu = 12$ . (b) Charge density profiles of all many-body states under PBC. (c) the same as (b) but for OBC. We consider  $L = 10$ ,  $N = 3$ ,  $U = 20t$  and a relatively large  $\gamma = 0.9t$  for better illustration.

Figure S6 plots the clusters for fixed  $N$  and increasing  $L$ . We see that as  $L$  grows, the eigenenergies fill the clusters more densely. In the TDL, the clusters form continuous areas and orbits in the complex-energy plane. Thus, we can always find a continuous orbit of eigenenergies that surround the energy center of any cluster. A nonzero topological invariant can be obtained as the winding numbers of these orbits. We note that the extents of the clusters (including the one at  $\varepsilon_1 = (N - 1)U$ ) on real and imaginary axes are independent of large  $L$ . The extents of the clusters are finite, provided that  $U$  is finite.

For single particles, it has been demonstrated that a nonzero spectral winding number inevitably lead to the non-Hermitian skin effect [14, 15]. In the following, we show that this relationship can be generalized to many-body strongly interacting systems. The point-gap topology with nonzero winding numbers in the PBC spectrum ensures that its difference as compared to the OBC one, thus leading to the non-Hermitian skin effect even in the many-body interacting systems.

We focus on the strong interaction ( $U \gg t$ ) regime where the PBC spectrum develops multiple clusters which are centered at  $\varepsilon_s \in \{0, U, \dots, (N - 1)U\}$  and have nonzero winding numbers, as we discussed before. In this strong interaction regime, we consider the kinetic hopping term

$$\hat{V}_h = \sum_{\ell=1}^L [(t + \gamma)\hat{c}_\ell^\dagger \hat{c}_{\ell+1} + (t - \gamma)\hat{c}_{\ell+1}^\dagger \hat{c}_\ell] \quad (\text{VIII1})$$

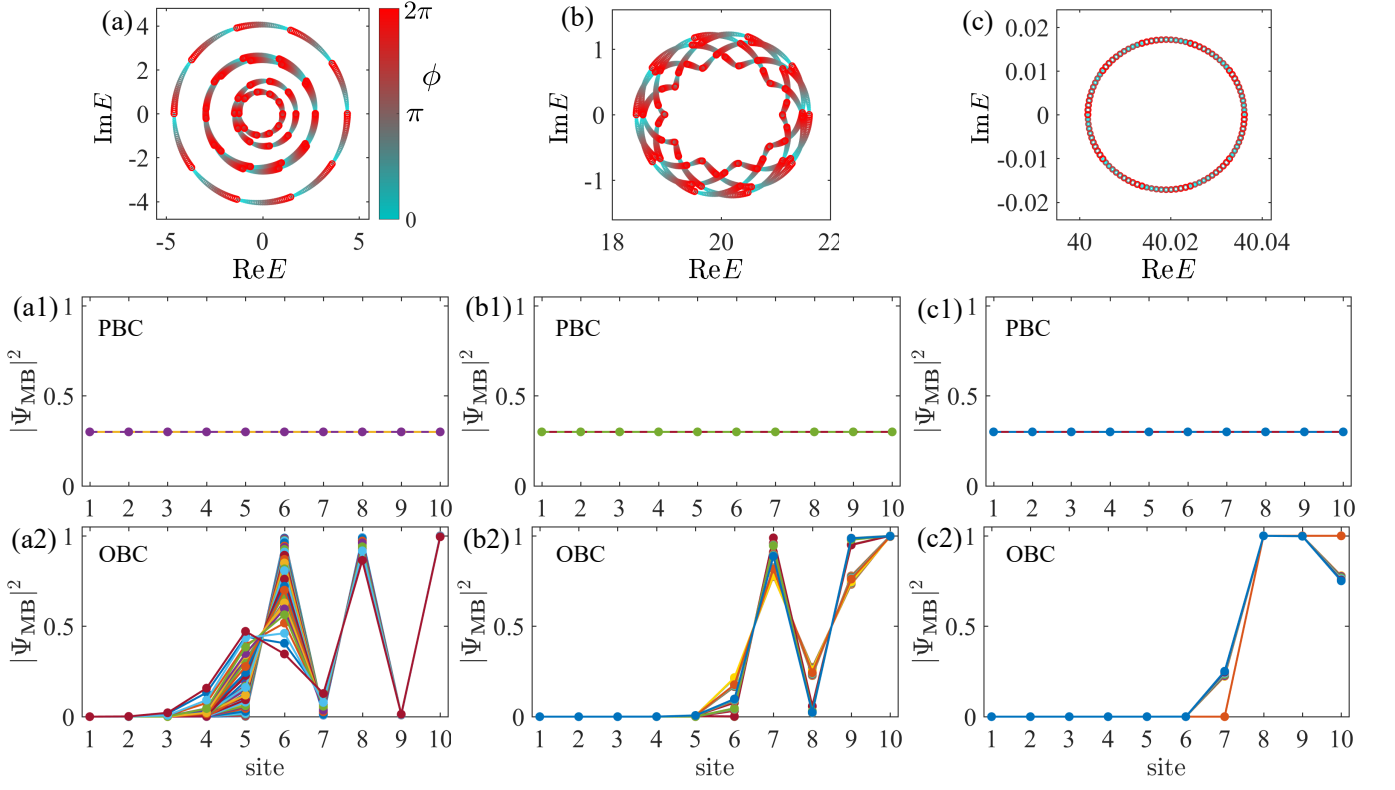


Fig. S5. (a-c) Movement of the eigenenergies of the clusters at  $\varepsilon_s = 0, U$  and  $2U$ , respectively, when the twist boundary angle  $\phi$  increases from 0 (cyan) to  $2\pi$  (red). All eigenenergies belonging to the same cluster wind around the center in one direction. The spectral winding numbers for the three clusters are found as  $\nu_s = 5, 4$  and  $3$ , respectively. (a1-c1) Charge density profiles of the eigenstates with energies around  $\varepsilon_s = 0, U$  and  $2U$ , respectively, when PBC are imposed. (a2-c2) the same as (a1-c1) but for OBC. The charge-density profiles are markedly different for PBC and OBC. Moreover, the charge densities tend to localize at one open boundary when OBC are imposed. Other parameters are the same as Fig. S4.

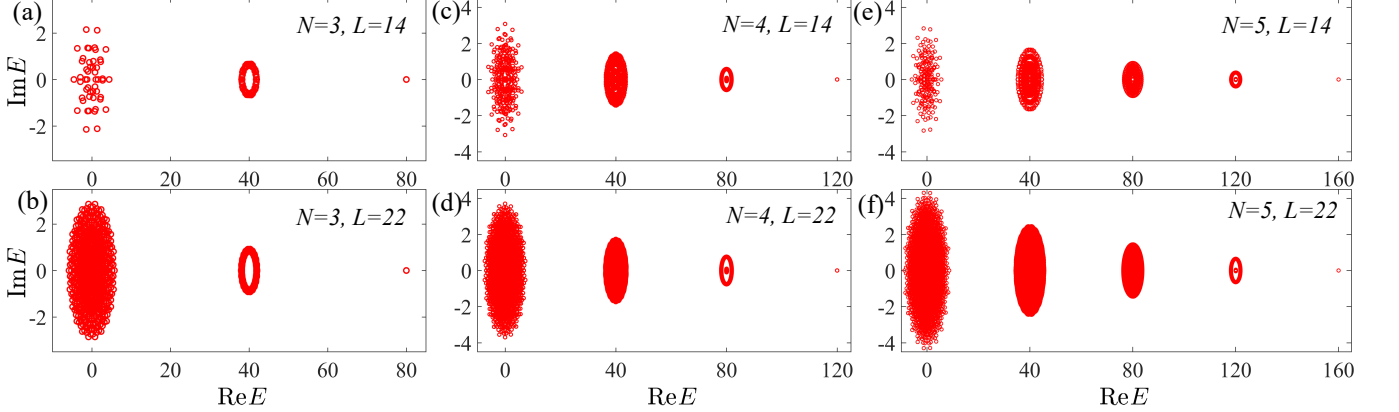


Fig. S6. Spectral clusters for fixed  $N$  and increasing  $L$ . The right, middle and left panels are for  $N = 3, 4$  and  $5$ , respectively. The upper and lower panels are  $L = 14$  and  $22$ , respectively. As  $L$  grows, the eigenenergies fill the clusters more densely. In the TDL, the clusters occupy continuous areas and orbits around their energy centers in the complex-energy plane.

as a perturbation to the unperturbed Hamiltonian which consists of only the interaction term

$$\hat{H}_{\text{int}} = U \sum_{\ell=1}^L \hat{n}_{\ell} \hat{n}_{\ell+1}. \quad (\text{VII2})$$

Then, up to the  $N$ -order perturbations in  $\hat{V}_h$ , the effective Hamiltonian projected within cluster  $s \in \{1, 2, \dots, N\}$  may

be written as

$$\hat{H}_{\text{eff}}^{(s)} = (N - s)U + \hat{P}_s \sum_{j=1}^N \hat{V}_h [(E - \hat{H}_{\text{int}})^{-1} \hat{V}_h]^{j-1} \hat{P}_s + \mathcal{O}(\hat{V}_h^{N+1}), \quad (\text{VII3})$$

where  $\hat{P}_s$  is the orthogonal projection operator onto the many-body Fock subspace associated with cluster  $s$ . Using the perturbation theory, we can derive effective Hamiltonians under PBC and OBC, respectively, for each cluster. From these Hamiltonians, we can find again that the PBC spectrum has a nonzero winding number whereas the OBC spectrum is always real, which is consistent with our numerical calculations. Indeed, the effective Hamiltonian under OBC can be converted into a Hermitian one via a similarity transformation. Such a similarity transformation does not change the spectrum, and clearly shows the concentration of the many-body eigenstates to the Fock basis state with its particles accumulated close to an open boundary. Therefore, the many-body eigen wavefunctions are localized to the boundary, thus exhibiting the many-body non-Hermitian skin effect.

As an illustration, we consider the cluster  $s = 1$ . For this cluster, we denote and order the orthogonal many-body basis with the position as

$$|\bar{\ell}\rangle = \hat{c}_\ell^\dagger \hat{c}_{\ell+1}^\dagger \dots \hat{c}_{\ell+N-1}^\dagger |\text{vac}\rangle, \quad \ell \in \{1, \dots, L\}, \quad (\text{VII4})$$

where  $|\text{vac}\rangle$  is the vacuum state. The effective Hamiltonian under PBC can be derived as

$$\langle \bar{j} | \hat{H}_{\text{eff}}^{(1)} | \bar{\ell} \rangle = \tilde{E}_1 \delta_{j,\ell} + \frac{(t - \gamma)^N}{U^{N-1}} \delta_{j,\ell+1} + \frac{(t + \gamma)^N}{U^{N-1}} \delta_{j,\ell-1}, \quad (\text{VII5})$$

where  $\tilde{\varepsilon}_1 = (N - 1)U + E_{1,c}$ . Thus, the effective Hamiltonian is given by

$$\hat{H}_{\text{PBC}}^{(1)} = \tilde{\varepsilon}_1 + \sum_{\ell=1}^L \left[ \frac{(t - \gamma)^N}{U^{N-1}} |\bar{\ell} + 1\rangle \langle \bar{\ell}| + \frac{(t + \gamma)^N}{U^{N-1}} |\bar{\ell}\rangle \langle \bar{\ell} + 1| \right]. \quad (\text{VII6})$$

This Hamiltonian takes a similar form as the single-particle Hatano-Nelson model but is defined on the basis of Fock states. In the  $N = 1$  limit, it recovers the single-particle Hamiltonian. The  $E_{\text{shift}}$  in Eq. (VII6) stems from the even-order corrections. It shifts the energy of the cluster globally in real axis and thus does not affect the topology of the system of interest. To the second-order corrections, the energy shift can be estimated as  $E_{1,c} \approx 2(t^2 - \gamma^2)/U$ . The hopping terms are dominated by the  $N$ -order correction. They are non-reciprocal in the orthogonal Fock subspace: the hopping amplitude from the many-body state  $|\bar{\ell}\rangle$  to the next one  $|\bar{\ell} + 1\rangle$  is  $(t - \gamma)^N/U^{N-1}$ , while the hopping amplitude for the inverse process is instead  $(t + \gamma)^N/U^{N-1}$ . By Fourier transformation, the energy spectrum can be found as

$$\tilde{E}_{\text{PBC}}^{(1)} = \tilde{\varepsilon}_1 + \frac{(t - \gamma)^N}{U^{N-1}} e^{-iq} + \frac{(t + \gamma)^N}{U^{N-1}} e^{iq}, \quad (\text{VII7})$$

where  $q \in \{0, 2\pi/L, 4\pi/L, \dots, 2\pi\}$  can be viewed as the momentum of the many-body eigenstates. This spectrum is consistent with the numerical calculations, as shown in Fig. S7. From Eq. (VII7), we also see that in the TDL ( $L \rightarrow \infty$ ), the spectrum forms a closed loop in the complex-energy plane, similar to that of the single-particle Hatano-Nelson model [cf. Fig. S7(b)]. Taking into account the magnetic flux, the spectrum becomes

$$\tilde{E}_{\text{PBC}}^{(1)}(\phi) = \tilde{\varepsilon}_1 + e^{-iN\phi/L} e^{-iq} + e^{iN\phi/L} e^{iq} \frac{(t + \gamma)^N}{U^{N-1}}. \quad (\text{VII8})$$

Using Eq. (3) in the main text, we obtain the winding number as  $\nu_1 = \text{sgn}(\gamma)N$ , which again is consistent with our numerical calculations [c.f. Fig. S7(c)].

Next, we impose OBC (i.e., termination of the coupling between the  $\ell = 1$  and  $L$  sites) and derive the effective Hamiltonian as

$$\hat{H}_{\text{OBC}}^{(1)} = \tilde{\varepsilon}_1 - \sum_{\ell=1}^{N-1} E_\ell (|\bar{\ell}\rangle \langle \bar{\ell}| + |\bar{L} - \ell\rangle \langle \bar{L} - \ell|) + \sum_{\ell=1}^{L-N} \frac{(t - \gamma)^N}{U^{N-1}} |\bar{\ell} + 1\rangle \langle \bar{\ell}| + \frac{(t + \gamma)^N}{U^{N-1}} |\bar{\ell}\rangle \langle \bar{\ell} + 1|. \quad (\text{VII9})$$

Note that under OBC, we have  $L - N + 1$  many-body states in cluster  $s = N$ . Due to the termination, the Fock basis states close to the two ends have different potential corrections compared to those deep in the bulk. Following the

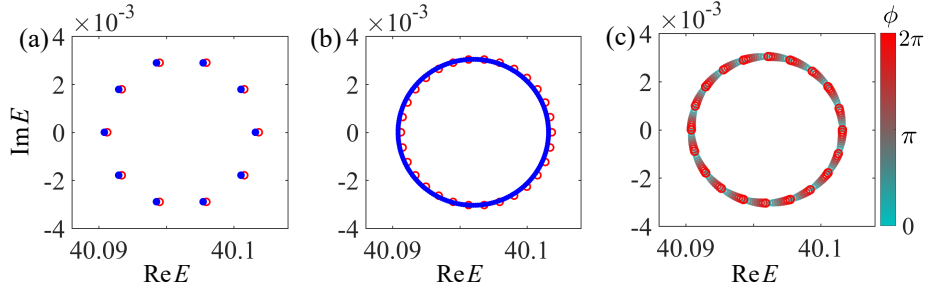


Fig. S7. (a) Many-body spectrum (blue) obtained by the effective model in Eq. (VII6). The red circles are obtained by exact diagonalizing the full many-body Hamiltonian and are plotted for comparison. (c) Many-body spectrum (blue) obtained by the effective model in Eq. (VII7) in the TDL. The red circles are obtained by exact diagonalizing the full many-body Hamiltonian with  $L = 30$  sites and are plotted for comparison. (c) Evolution of many-body spectrum (blue) obtained by the effective model in Eq. (VII8) by increasing the twist angle  $\phi$  from 0 to  $2\pi$ . We consider  $N = 3$ ,  $\gamma = 0.2t$ ,  $U = 20t$ ,  $t = 1$ ,  $s = 1$  and PBC in all panels, and  $\phi = 0$  in (a) and (b).

spirit of Refs. [14, 15], one can show that the Hamiltonian with open boundaries is always topological trivial in terms of point gaps. To be explicit, we can apply a similarity transformation

$$|\bar{\ell}\rangle \rightarrow \eta^\ell |\bar{\ell}\rangle, \quad \langle \bar{\ell}| \rightarrow \eta^{-\ell} \langle \bar{\ell}|, \quad (\ell \in \{1, \dots, L - N + 1\}), \quad (\text{VII10})$$

where  $\eta = |(t + \gamma)/(t - \gamma)|^{N/2}$ , and transfer the Hamiltonian (VII9) to a Hermitian one

$$\hat{H}_{\text{OBC}}^{(1)'} = \tilde{\varepsilon}_1 - \sum_{\ell=1}^{N-1} E_\ell (|\bar{\ell}\rangle \langle \bar{\ell}| + |\overline{L-\ell}\rangle \langle \overline{L-\ell}|) + \frac{(t^2 - \gamma^2)^{N/2}}{U^{N-1}} \sum_{\ell=1}^{L-N} (|\bar{\ell} + 1\rangle \langle \bar{\ell}| + |\bar{\ell}\rangle \langle \bar{\ell} + 1|). \quad (\text{VII11})$$

The similarity transformation does not change the spectrum. Thus, the effective Hamiltonian (VII9) under OBC has a purely real spectrum, topologically different from that under PBC. In the TDL, we approximate the spectrum as

$$\tilde{E}_{\text{OBC}}^{(1)} \approx \tilde{\varepsilon}_1 + 2 \frac{(t^2 - \gamma^2)^{N/2}}{U^{N-1}} \cos q, \quad (\text{VII12})$$

where  $q \in \{0, 2\pi/(L - N + 1), 4\pi/(L - N + 1), \dots, 2\pi\}$ . The OBC spectrum forms a line in real axis inside the PBC spectrum (i.e., closed loop) (see Fig. S8). This result indicates that most and extensive many-body eigenstates under OBC are localized to one open boundary. These results are also consistent with our numerical calculations.

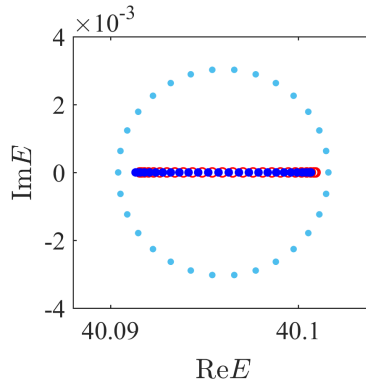


Fig. S8. (a) Many-body spectrum (blue dots) obtained by the effective model in Eq. (VII9). The red circles are obtained by exact diagonalizing the full many-body Hamiltonian. The cyan dots are the spectrum under OBC. Other parameters are the same as those in Fig. S7.

In fact, from the similarity transformation, we can further see that for  $N \ll L$ , the many-body eigenstates tend to concentrate to the Fock basis state  $|\overline{L - N + 1}\rangle$  if  $|\eta| > 1$  while to the state  $|\bar{1}\rangle$  if  $\eta < 1$ . Note that the wavefunction of the basis state  $|\bar{\ell}\rangle$  are accumulated from sites  $\ell$  to  $\ell + N - 1$ . Thus, the many-body eigen wavefunctions are



localized at the right end if  $\eta > 1$  while at the left end if  $\eta < 1$ . When  $\gamma = 0$ , the spectral winding numbers become ill-defined. Accordingly, the similarity transformation become trivial with  $\eta = 1$ , and thus the many-body skin effect disappears. From this aspect, we see clearly that the nontrivial spectral winding number and the many-body skin effect are intimately related.

The above derivation can be generalized to other clusters, which is relatively more complicate. However, the essential results are the same: the many-body system can be understood as a "single-particle" model defined on the basis of Fock states, and the OBC effectively terminate the direct coupling between the "boundary" Fock basis states whose particles accumulated towards the boundaries. The nontrivial spectral topology of the PBC spectrum leads to the localization of the many-body eigenstates to the boundary Fock states, in the same manner as that in single-particle system, which hence exhibit the localization of the many-body eigen wavefunctions towards the boundaries. Finally, it may be also worth noting that for other clusters, the non-reciprocal hopping between the Fock basis states can be obtained by lower-order corrections. Thus, we find stronger effective nonreciprocity and hence larger spectral areas for these clusters. This is also confirmed by our numerical observations [Fig. 4(b) in the main text].

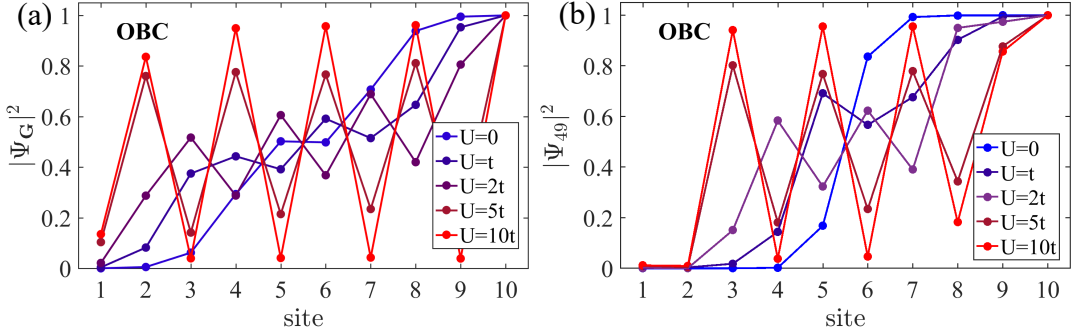


Fig. S9. Charge-density profiles of many-body states for  $U = 0, t, 2t, 5t$  and  $10t$ , respectively. Two states, namely, (a) the ground state and (b) the 50th lowest- $\text{Re}(E)$  states, are taken for illustrations. With increasing  $U$ , the charge-density profile of the many-body states become extended over the whole lattice chain with open boundaries.  $L = 10, N = 5$  and other parameters are the same as Fig. S5

In contrast, at half-filling and for  $|\gamma| < t$  ( $|\gamma| > t$ ), the many-body spectrum of a finite system under PBC shrinks onto the real axis (open lines parallel to the imaginary axis) as  $U$  increase. Accordingly, we observe that upon increasing  $U$ , the charge-density profile of the many-body states become extended over the whole lattice chain with open boundaries, as shown in Fig. S9. For concreteness and brevity, we show the results for two states in Fig. S9. We note that all other many-body states exhibit similar behaviors.

### Appendix VIII: Other half-filled cases

In the main text, we have discussed (I) the half-filled cases with odd (even)  $N = L/2$  and (anti-)PBC. In this section, we discuss the results for the complementary half-filled cases (II), namely, with even (odd)  $N$  and (anti-)PBC. In the cases (II), the system has always two ground states with complex-conjugate energies; and there is no exceptional point between two lowest excited states, as shown in Figs. S10(a) and (b). Thus, we do not observe the two  $\mathcal{PT}$  transitions. However, we observe that as the size of the system  $L$  grows, the excitation gap  $\Delta_{\text{gap}}$  becomes vanishingly small for  $U < U'_c$  and increases rapidly for  $U > U'_c$ , and the critical interaction strength  $U'_c$  approaches with that one ( $U_c$ ) characterizing the low-energy  $\mathcal{TP}$  transition in the cases (I) [cf. Fig. S10(c)]. This result indicates that in the TDL, the phase transition from the gapless regime to the gapped CDW regime happens also in the cases (II) and the corresponding critical interaction strength coincides with that in the cases (I).

### Appendix IX: Calculations for the non-Hermitian SSH-type model

Our main results, such as the symmetry-breaking phase transitions and nontrivial spectral topology, revealed from the interacting Hatano-Nelson model are general. They can also be applied to other models. As an example,

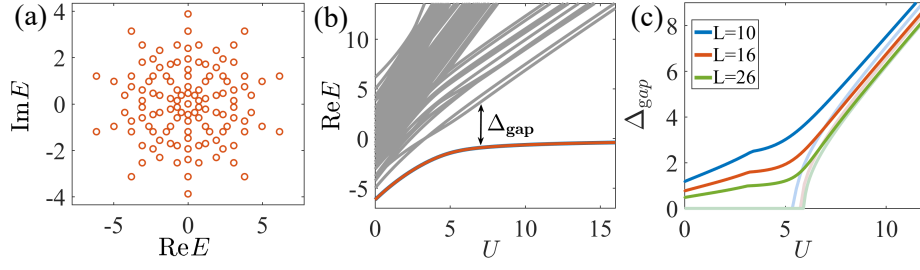


Fig. S10. Results for the cases with even (odd)  $N = L/2$  and (anti-)PBC. (a) Many-body spectrum at half-filling in the absence of interactions ( $U = 0$ ). (b) Real part of the low-energy many-body spectrum as a function of  $U$ . We take  $L = 10$  for illustration. (c) Excitation gap  $\Delta_{\text{gap}}$  as a function of  $U$ . The light colored lines are the results for cases (I) and presented here for comparison. We see that as  $L \rightarrow \infty$ , the metal-insulator transition in cases (II) resemble that in cases (I). Other parameters are the same as that in Fig. 3 in the main text, namely  $L = 10$  in panels (a) and (b), and  $\gamma = 0.6t$  in all panels.

we consider the Su-Schrieffer-Heeger (SSH) type model in which non-reciprocal hopping occurs every two nearest-neighbour bonds, as sketched in Fig. S11(a). The non-Hermitian SSH-type Hamiltonian reads

$$H = \sum_{\ell} \left\{ (\hat{C}_{\ell}^{\dagger} (t\sigma_x - i\gamma\sigma_y) \hat{C}_{\ell} + \frac{t}{2} [\hat{C}_{\ell+1}^{\dagger} (\sigma_x + i\sigma_y) \hat{C}_{\ell} + h.c.]) \right\}, \quad (\text{IX1})$$

where  $\hat{C}_{\ell} \equiv (\hat{c}_{A,\ell}, \hat{c}_{B,\ell})^T = (\hat{c}_{2\ell-1}, \hat{c}_{2\ell})^T$  with  $A$  and  $B$  indicating odd and even lattice sites, respectively. The Pauli matrices act on sublattice space consisting of  $A$  and  $B$ .  $h.c.$  indicates Hermitian conjugation of the previous term. Figure S11(c) illustrates the flow of the full spectrum of the model with size  $L = 12$  and half-filling under anti-PBC. We see clearly that both the low-energy and full  $\mathcal{PT}$  phase transitions occurs in the non-Hermitian SSH-type model as we increase the strength of nearest neighbor interaction. We have also checked that as  $L$  increases, while the critical strength  $U_{c,all}$  for the full  $\mathcal{PT}$  transition increases monotonically, the critical strength  $U_c$  for the low-energy  $\mathcal{PT}$  transition saturates to a finite value. The non-Hermitian SSH-type model also exhibits the nontrivial winding in the spectrum, as shown in Fig. S12. All these features are the same as those in the interacting Hatano-Nelson model (up to that the imaginary energies are half of those of the Hatano-Nelson model).

It may be worthy noting that through a local unitary transformation  $\hat{C}_{\ell} \rightarrow 1/\sqrt{2}(\sigma_0 + i\sigma_x)\hat{C}_{\ell}$ , the model (IX1) can be converted to a Creutz-ladder-like model [12]

$$H = \sum_{\ell} \left\{ (\hat{C}_{\ell}^{\dagger} (t\sigma_x + i\gamma\sigma_z) \hat{C}_{\ell} + \frac{t}{2} [\hat{C}_{\ell+1}^{\dagger} (\sigma_x - i\sigma_z) \hat{C}_{\ell} + h.c.]) \right\}. \quad (\text{IX2})$$

Notably, the non-Hermiticity in the Creutz-ladder-like model contains pure onsite gain ( $i\gamma$ ) and loss ( $-i\gamma$ ) [see Fig. S11(a)]. The interaction term can be transformed accordingly and remains Hermitian after the transformation.

The dissipative Hamiltonian (IX2) can be directly derived from the Lindblad equation as we show in the following. The Lindblad equation under the Markov approximation reads [100]

$$\frac{d\rho}{dt} = -i[H_0, \rho] + \sum_{\ell} \left( L_{\ell} \rho L_{\ell}^{\dagger} - \frac{1}{2} \{L_{\ell}^{\dagger} L_{\ell}, \rho\} \right), \quad (\text{IX3})$$

where  $\rho(t)$  is the density matrix of the system at time  $t$ .  $H_0$  is the system Hamiltonian in the absence of coupling to environment. It is Hermitian and prepared as

$$H_0 = \sum_{\ell} t \left\{ \hat{C}_{\ell}^{\dagger} \sigma_x \hat{C}_{\ell} + \frac{1}{2} [\hat{C}_{\ell+1}^{\dagger} (\sigma_x - i\sigma_z) \hat{C}_{\ell} + h.c.] \right\}. \quad (\text{IX4})$$

$L_{\ell}$  are the Lindblad jump operators in terms of fermion operators. We consider one-body loss events described by  $L_{\ell} = g_{\ell} \hat{c}_{\ell}$  with  $g_{\ell} = i^{\ell} \sqrt{2\gamma}$ . The coefficients  $g_{\ell}$  are determined from the loss rates of atoms. Following the quantum trajectory method [101], the dynamics of the system can be decomposed into a Schrödinger evolution under an effective non-Hermitian Hamiltonian and quantum-jump processes which induce particle losses with the jump operators  $L_{\ell}$ ,

$$\frac{d\rho}{dt} = -i(H_{\text{eff}}\rho - \rho H_{\text{eff}}^{\dagger}) + \sum_{\ell} L_{\ell} \rho L_{\ell}. \quad (\text{IX5})$$

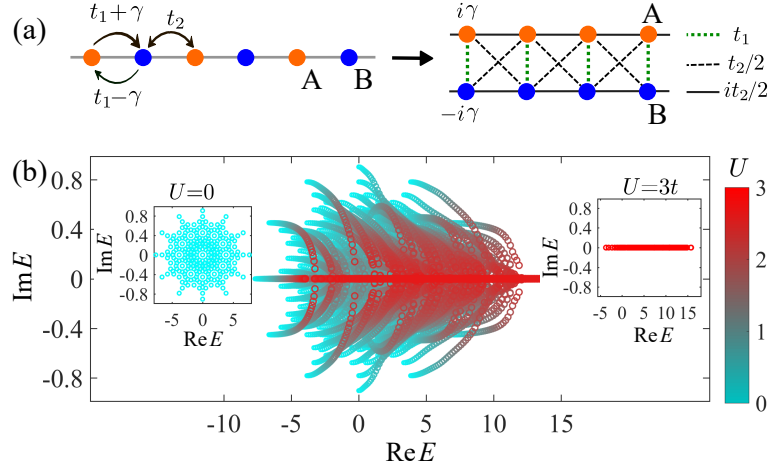


Fig. S11. (a) Schematic for the non-Hermitian SSH-type model (left panel). The orange and blue dots indicate two sublattices ( $A$  and  $B$ ), respectively. The nonreciprocal hopping occurs only within unit cells. The model can be converted to a Creutz-ladder-like model with imaginary hopping and onsite gain and loss (right panel). (b)  $\mathcal{PT}$  transitions in the interacting non-Hermitian SSH-type lattice chain with  $L = 12$ ,  $N = 6$  and  $\gamma = 0.2t$ . The changing colour (from cyan to red) indicates the change of interaction strength from  $U = 0$  to  $3t$ . The insets show the spectra at  $U = 0$  and  $3t$ , respectively. We consider anti-PBC for illustration.

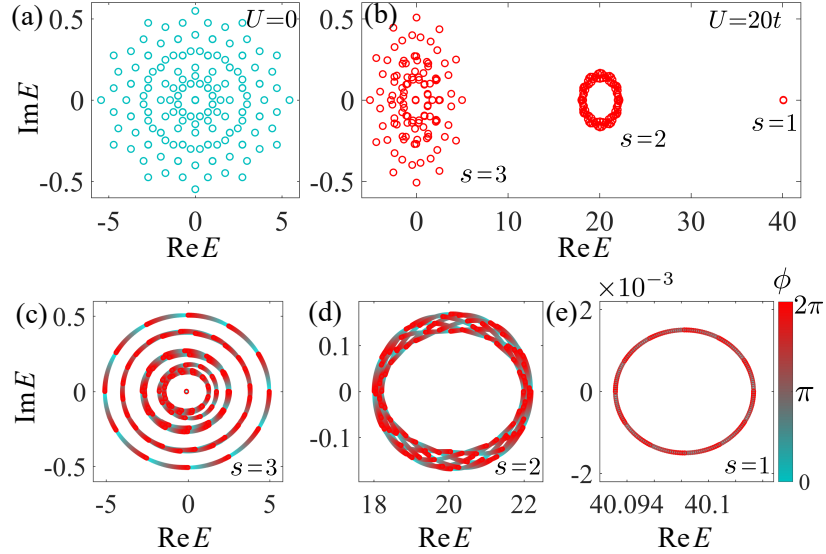


Fig. S12. Energy spectrum of the interacting SSH-type lattice chain with  $L = 12$ ,  $N = 3$  and  $\gamma = 0.2t$ . (a) and (b) are the spectra at  $U = 0$  and  $20t$  respectively. (c), (d) and (e) display respectively the movement of the three spectral clusters (labeled by  $s = 1, 2, 3$ ) as varies  $\phi$  from 0 (cyan) to  $2\pi$  (red).

We find that the resulting effective Hamiltonian

$$H_{\text{eff}} = H_0 - \frac{i}{2} \sum_{\ell} L_{\ell}^{\dagger} L_{\ell} = H_0 + i\gamma \sum_{\ell} \hat{C}_{\ell}^{\dagger} \sigma_z \hat{C}_{\ell} \quad (\text{IX6})$$

gives exactly the dissipative Creutz model in Eq. (IX2). It describes the evolution of the system during a time interval between quantum jump events. If we consider a situation where the equilibration time in the measured many-body system is shorter than a typical time between quantum jumps, it is justified to consider only  $H_{\text{eff}}$  for the short-time evolution.